

PHOTOELECTRON IMAGING SPECTROSCOPY  
OF  
INTERMOLECULAR INTERACTIONS  
IN  
CLUSTER ANIONS

by

Yerbolat Dauletyarov

---

Copyright © Yerbolat Dauletyarov 2022

A Dissertation Submitted to the Faculty of the  
DEPARTMENT OF CHEMISTRY AND BIOCHEMISTRY

In Partial Fulfillment of the Requirements

For the Degree of

DOCTOR OF PHILOSOPHY

IN PHYSICAL CHEMISTRY

In the Graduate College

THE UNIVERSITY OF ARIZONA

2022

THE UNIVERSITY OF ARIZONA  
GRADUATE COLLEGE

As members of the Dissertation Committee, we certify that we have read the dissertation prepared by: Yerbolat Dauletyarov,  
titled: Photoelectron Imaging Spectroscopy of Intermolecular Interactions in Cluster Anions,  
and recommend that it be accepted as fulfilling the dissertation requirement for the Degree of Doctor of Philosophy.

  
\_\_\_\_\_  
Andrei Sanov Date: May 2, 2022

  
\_\_\_\_\_  
Oliver Monti Date: May 2, 2022


  
\_\_\_\_\_  
Steven Schwartz Date: May 2, 2022

  
\_\_\_\_\_  
Dennis Lichtenberger Date: May 2, 2022

Final approval and acceptance of this dissertation is contingent upon the candidate's submission of the final copies of the dissertation to the Graduate College.

I hereby certify that I have read this dissertation prepared under my direction and recommend that it be accepted as fulfilling the dissertation requirement.



  
\_\_\_\_\_  
Andrei Sanov Date: May 11, 2022  
Dissertation Committee Chair  
Department of Chemistry and Biochemistry

ARIZONA

# Acknowledgements

I would like to thank my dissertation committee members for their guidance and encouragement. Especially, my advisor, Andrei Sanov, for being patient with me through all these years, overlooking my flaws, and thus allowing me to develop in my own manner and at my own pace.

My sincere gratitude goes to all members of Sanov group, with whom I have interacted as a graduate student at CBC. To Andrew Dixon, who taught me how to operate the photoelectron imaging spectrometer. To Adam Wallace, with whom I have spent countless hours fixing it and trying to get experiments working. To Christopher Blackstone, who did a great job preparing me for my oral exam. To Beverly Ru, who was always around to lend a hand in times of need.

I would like to extend my gratitude to my undergraduate advisor, Sergiy Bubin, who set me on a path to becoming a physical chemist.

A special thanks goes to my close friend, Rustam Gatamov, whose childish enthusiasm for pretty much everything was a source of many invigorating discussions that kept my spirits high.

I am deeply grateful to my wonderful wife and my amazing children. Your love and care helped me to endure through this.

# Dedication

*I dedicate this work to my parents.  
May God be always with you.*

# Contents

<b>List of Figures</b>	<b>7</b>
<b>List of Tables</b>	<b>9</b>
<b>Abstract</b>	<b>10</b>
<b>Chapter 1: Introduction</b>	<b>12</b>
<b>Chapter 2: Instrumentation and experimental design</b>	<b>16</b>
2.1 Vacuum system . . . . .	17
2.2 Ion production . . . . .	17
2.3 Time-of-flight mass spectrometer . . . . .	19
2.4 Laser system . . . . .	21
2.5 Velocity map imaging assembly . . . . .	21
<b>Chapter 3: Methylglyoxal</b>	<b>24</b>
3.1 Experimental results . . . . .	26
3.2 Theory vs Experiment: structures . . . . .	27
3.3 Theory vs Experiment: energies . . . . .	30
3.4 Theory vs Experiment: Franck-Condon simulation . . . . .	35
3.5 Summary . . . . .	35
<b>Chapter 4: Biacetyl and its cluster anions</b>	<b>38</b>
4.1 Experimental results: biacetyl anion . . . . .	39
4.2 Experimental results: cluster anions of biacetyl . . . . .	40

4.3	Theory vs Experiment: biacetyl anion . . . . .	42
4.3.1	Structures . . . . .	42
4.3.2	Energies . . . . .	44
4.4	Theory vs Experiment: cluster anions of biacetyl . . . . .	50
4.4.1	Structures . . . . .	50
4.4.2	Energies . . . . .	52
4.5	Conclusions . . . . .	57
<b>Chapter 5: Oxalyl chloride</b>		<b>60</b>
5.1	Geometric structures . . . . .	61
5.2	Experimental results . . . . .	64
5.3	Electronic structure . . . . .	69
5.3.1	Bound States . . . . .	69
5.3.2	Anionic Resonances . . . . .	71
5.4	Photoelectron angular distributions . . . . .	73
5.5	Comparison to other anions in the glyoxal family . . . . .	76
5.6	Summary . . . . .	77
<b>Chapter 6: Summary and future directions</b>		<b>82</b>
<b>Bibliography</b>		<b>84</b>

# List of Figures

1.1	Small dicarbonyls . . . . .	14
3.1	Methylglyoxal: photoelectron spectra . . . . .	28
3.2	Methylglyoxal: structures . . . . .	31
3.3	Methylglyoxal: molecular orbitals . . . . .	36
3.4	Methylglyoxal: Franck-Condon simulation . . . . .	36
4.1	Biacetyl: photoelectron spectrum . . . . .	45
4.2	Solvated clusters of biacetyl: photoelectron spectra . . . . .	46
4.3	Cluster anions of biacetyl: photoelectron spectra . . . . .	47
4.4	Biacetyl: structures . . . . .	48
4.5	Biacetyl dimer: structures . . . . .	53
4.6	Biacetyl trimer: structure . . . . .	54
4.7	Cluster anions of biacetyl: molecular orbitals . . . . .	55
4.8	Biacetyl dimer: energy diagram . . . . .	59
5.1	Oxalyl chloride: molecular orbitals . . . . .	65
5.2	Oxalyl chloride: energy diagram . . . . .	66
5.3	Oxalyl chloride: mass spectrum . . . . .	79
5.4	Oxalyl chloride: photoelectron spectra . . . . .	80

5.5 Oxalyl chloride: anisotropy parameter vs electron kinetic energy . . . . .	81
5.6 Comparison of the photoelectron spectra of small dicarbonyls . . . . .	81

# List of Tables

3.1	Methylglyoxal: structures . . . . .	32
3.2	Methylglyoxal: energies . . . . .	34
4.1	Biacetyl: structures . . . . .	45
4.2	Biacetyl: energies . . . . .	54
4.3	Cluster anions of biacetyl: energies . . . . .	58
5.1	Oxalyl chloride: structures . . . . .	65
5.2	Oxalyl chloride: energies at <i>trans</i> and <i>anti</i> geometries . . . . .	74
5.3	Oxalyl chloride: energies at <i>cis</i> geometry . . . . .	75

# Abstract

The heart of this dissertation is an experimental study of biacetyl (BA) and its smaller cluster anions,  $(\text{BA}_n)^-$  where  $n = 2 - 4$ , conducted using photoelectron imaging spectroscopy. Large band shifts between photoelectron spectra of cluster anions of nonpolar BA, comparable or sometimes even larger than the shift caused by solvation of BA by very polar water molecule, led us to hypothesize that interactions between BA molecules are of weak covalent nature. In other words, in  $(\text{BA}_n)^-$  there is a significant degree of charge delocalization, in contrast to a typical cluster anion, that is held together due to electrostatic interactions between the cluster core, holding the excess charge, and surrounding neutral solvent molecules. In order to support experimental findings, we performed geometry optimization calculations using *ab initio* methods for BA, and DFT method for the cluster anions. The results were quite successful in explaining the features of photoelectron spectra. Especially for BA the agreement between the experiment and theory was excellent. Furthermore, the *ab initio* calculations showed that the HOMO of BA anion has high charge density with  $\pi$  bonding character along the central C-C bond, which facilitates charge delocalization in the cluster anions, as revealed by DFT results. Specifically, sandwich-like structures of  $\text{BA}_2^-$  and  $\text{BA}_3^-$ , enabled by flat geometry of BA, are held together by

$\pi - \pi$  intermolecular interactions.

The study of BA and its cluster anions is complemented by the photoelectron imaging spectroscopy studies of electronic structures of methylglyoxal and oxalyl chloride. We characterize their several lowest electronic states and determine their electron affinities (EA) for the first time. The results are discussed in the context of the substitution series (Figure 1.1), which includes glyoxal, methylglyoxal (single methyl substitution), biacetyl (double methyl substitution), and oxalyl chloride (double chlorine substitution). The EAs and anion detachment energies follow the trend: biacetyl < methylglyoxal < glyoxal  $\ll$  oxalyl chloride. The electron-donating character of the methyl group has a destabilizing effect on the substituted anions, reducing the EA from glyoxal to methylglyoxal to biacetyl. In contrast, the strong electron-withdrawing power of Cl lends additional stabilization to the oxalyl chloride anion, resulting in a large ( $\sim 1$  eV) increase in its detachment energy compared to glyoxal.

# Chapter 1

## Introduction

Scientific reductionism, a methodology of explaining the behavior of complex systems in terms of the behavior of its constituents, is a hallmark of physical sciences. Even though emergent phenomena are almost impossible to anticipate theoretically and almost always first discovered experimentally [1], their complete understanding is achieved by viewing them as a result of fundamental interactions between elementary constituents of a system.

Since the building blocks of most chemical systems are molecules, the deep insight into chemistry is gained by studying the nature of intermolecular interactions [2]. For an accurate and reliable investigation of intermolecular interactions, it is important to avoid external interference and effects of statistical averaging. In other words, a system under study must be relatively small, well-defined, and isolated. Nonetheless, it is not right to limit the study to pairwise interactions only, because increasing the size of a system introduces unexpected behavior. As

we know, even in classical physics, switching from two bodies to three bodies makes a system much more complex introducing deterministic chaos [3].

Clusters are perfect systems to study intermolecular interactions, possessing all three aforementioned properties [4]. In terms of their size, clusters are small enough to allow resolving interactions, which hold them together and are responsible for their structure and stability. Furthermore, modern ion production and mass spectrometry techniques allow creation of clusters of continuously varying sizes, so that it is possible to investigate how the nature of intermolecular interactions evolves as a function of cluster size. In this sense, clusters are intermediate states of matter situated between gas and condensed phases.

Historically, the first experimental study of clusters was presented by none other than Faraday in his 1857 lecture "Experimental relations of gold to light" [5]. Till the middle of the twenties century, clusters were mostly studied in the context of nucleation processes related to formation of clouds, fogs, and smokes [4]. The turning point in cluster science came in 1961, when Bentley [6] and Henkes [7] produced cluster cations of carbon dioxide using a supersonic nozzle and a mass spectrometer. Later in 1970s, with the advent of lasers and their usage to study clusters, cluster science was firmly established as a scientific field [4].

One of the branches of cluster science is a field of cluster anions [8], where the presence of the excess electron lends to a system a richer structure. In general, a cluster anion consists of the charged core, holding the excess electron, and neutral molecules, surrounding the core and acting as solvents. One of the main questions in the field of cluster anions is about the ex-

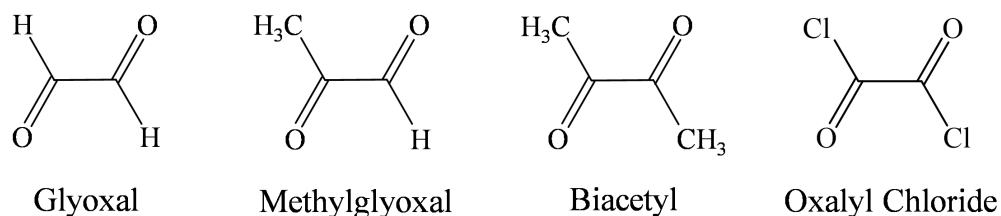


Figure 1.1: Small dicarbonyls

tent of delocalization of the excess electron. In other words, how many molecules is the cluster core going to consist of? Fundamentally, the question is about competition between charge delocalization and solvation interactions. On the one hand, the smaller core maximizes the interaction with the solvent molecules, due to its high charge density, thus lowering the total energy of the system. On the other hand, the charge delocalization lowers the total energy of the system due to weakly covalent bonds between molecules constituting the core. The answer is somewhat complicated and depends on specific properties of a cluster anion under study. It is best to illustrate the complexity through a classic and well-studied example of  $(\text{CO}_2)_n^-$  cluster series [9–14]. For  $n = 2 - 5$ , the excess electron is delocalized over two  $\text{CO}_2$  molecules forming a weak covalent bond between them. The rest of the  $\text{CO}_2$  molecules act as solvents surrounding the charged core. At  $n = 6$ , the cluster series partially undergoes so-called "core switching", monomer-based,  $\text{CO}_2^-(\text{CO}_2)_5$ , and dimer-based,  $(\text{CO}_2)_2^-(\text{CO}_2)_4$ , species coexisting. At  $n = 7$ , the clusters are completely monomer-based. This trend continues until  $n = 14$ , when it again becomes energetically more favorable to maintain dimer anion core. The "core switches" manifest themselves through photoelectron spectroscopy as discontinuities in the series of corresponding vertical detachment energies (VDEs).

In this dissertation, we present photoelectron imaging spectroscopic study of smaller cluster

anion,  $(BA_n)^-$  where  $n = 2 - 4$ , of biacetyl (BA) (Figure 1.1) [15]. Based on the analysis of photoelectron spectra, we hypothesize that the excess charge is delocalized over the whole cluster. We closely investigate the phenomenon computationally for  $n = 2, 3$ , confirming the hypothesis. Furthermore, we propose an explanation of how the HOMO of the biacetyl anion facilitates the charge delocalization in the clusters.

In addition to cluster anions of biacetyl, we present comparative photoelectron imaging spectroscopic study of the substitution series (Figure 1.1), which includes glyoxal [16], methylglyoxal [17] (single methyl substitution), biacetyl [15] (double methyl substitution), and oxalyl chloride [18] (double chlorine substitution).

## Chapter 2

# Instrumentation and experimental design

This dissertation is based on experiments conducted in Dr. Sanov's lab at the University of Arizona. Specifically, the negative-ion photoelectron imaging spectrometer was used to obtain all the photoelectron images of molecular and cluster anions of interest. It was built by former PhD students in Dr. Sanov's lab, Terefe Habteyes and Luis Velarde, whose dissertations [19, 20] contain more detailed description.

The photoelectron imaging spectrometer is a time-of-flight mass spectrometer coupled with photoelectron velocity map imaging assembly. A single experimental run on the instrument consists of four main steps:

- Production of anions
- Creation of a beam of anions and separating them in time according to their masses
- Timed laser interrogation of anions of interest and resulting electron detachment

- Velocity map imaging of photoelectrons

The following sections describe each step in detail.

## **2.1 Vacuum system**

The photoelectron imaging spectrometer runs under high vacuum. The instrument consists of three regions maintained under different pressures: source chamber, ion-optics region, and detection region. In a typical experiment the pressure in the source chamber is about  $3 \times 10^{-5}$  Torr. In the ion-optics and detection regions the pressures are on the order of  $10^{-6}$  and  $10^{-7}$  Torr, respectively.

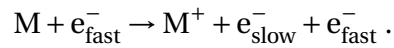
The source chamber and the ion-optics region are connected by a 4 mm diameter aperture. The ion-optics and detection regions are separated by a pneumatic gate valve. The source chamber is pumped by a 10" diffusion pump. The ion optics region is pumped by two turbomolecular pumps. The detection region is pumped by one turbomolecular pump. All the pumps are backed by mechanical roughing pumps.

## **2.2 Ion production**

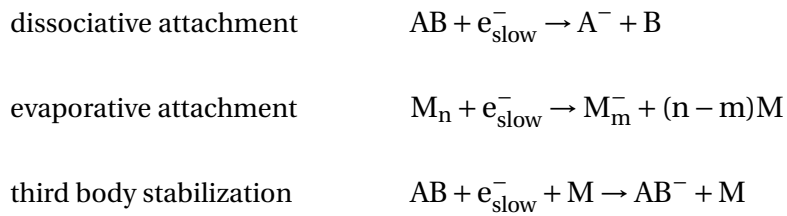
Ions are produced inside the source chamber by bombarding with electrons a jet of gas mixture from a pulsed valve (General Valve Series 9, Parker, Inc.). The gas mixture is formed outside the

source chamber by diffusing vapors of an appropriate chemical (in a liquid or powder form) with a carrier gas (typically Ar, N<sub>2</sub>, O<sub>2</sub>, CO<sub>2</sub>, or N<sub>2</sub>O) at absolute pressures of about 2 to 4 atm. The electrons are produced through thermionic emission by passing electric current through a thoria coated metal filament.

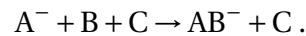
The collision of high energy electrons with molecules in the jet produces slow secondary electrons:



The slow secondary electrons are captured by molecules and molecular clusters through various energy dissipation mechanisms [21]:



Furthermore, the resulting anions participate in association reactions:



## 2.3 Time-of-flight mass spectrometer

The source chamber is connected to a Wiley-McLaren [22] time-of-flight mass spectrometer, which is coupled to a photoelectron velocity map imaging assembly [23]. The mass spectrometer forms a beam of anions separated in time according to their mass-to-charge ratios, thereby facilitating timed laser interrogation of anions of interest.

Anions produced in the source chamber are extracted into the ion-optics region by a repeller plate pulsed at an appropriate time from ground potential to approximately  $V_{\text{rep}} = -900$  V. After entering the ion-optics region the anions are further accelerated to approximately  $V_{\text{float}} \approx 2.5$  kV using evenly spaced serially connected (through 1 M $\Omega$  resistors) stack of 10 ring electrodes. Next, horizontal and vertical deflectors are used to steer the trajectories of the anions. Each deflector consists of two plates on opposite sides of the ion path with potential difference of about  $-100$  V to  $100$  V with respect to  $V_{\text{float}}$ . Afterward, the beam of anions is focused using an einzel lens consisting of three cylindrical electrodes. The potential on the first and last electrodes is  $V_{\text{float}}$ , whereas the potential on the middle electrode is about  $-1$  kV with respect to  $V_{\text{float}}$ . After focusing, the anions pass through a cylindrical tube initially floated at  $V_{\text{float}}$ , which switches back to ground potential before the anions exit it. Thus, the anions are referenced back to ground potential without changing their kinetic energy. The rest of the distance toward the detector the anions travel in a field-free region. The ratio  $V_{\text{float}}/V_{\text{rep}}$  is chosen so that ions of the same mass-to-charge ratio arrive at the detector at approximately the same time regardless of their initial positions and velocities.

The time  $t$  needed to cover a field-free distance  $d$  by an ion previously accelerated to potential  $V$  is directly proportional to the square root of its mass-to-charge ratio  $m/q$ :

$$t = \frac{d}{v} = d \left( \frac{m}{2KE} \right)^{1/2} = d \left( \frac{m}{2Vq} \right)^{1/2}$$

In other words, anions with the same mass-to-charge ratio arrive at the detector at the same time. So the time-of-flight mass spectrometer produces a time spectrum where every peak corresponds to species with the same mass-to-charge ratio. In reality, the contribution of multiply-charged anions to time spectrum is negligible, since their formation probability is much lower than that of singly-charged anions. So it is safe to assume that  $q = -e$ .

In practice, we determine the relationship between mass and time by fitting a straight line

$$t = c\sqrt{m} + t_0$$

to two time peaks of known masses (for example,  $O^-$  and  $O_2^-$ ). Mass spectrum  $g(m)$  is determined from time spectrum  $f(t)$  as follows:

$$g(m) = f(t) \frac{dt}{dm} = \left( \frac{c}{2} \right) \frac{f(c\sqrt{m} + t_0)}{\sqrt{m}}.$$

## 2.4 Laser system

Spectra Physics LAB-130-50 Nd:YAG pulsed laser with pulse width of 6-9 ns was used for all the experiments. The fundamental wavelength of the laser is 1064 nm. The wavelengths of 532 nm, 355 nm, and 266 nm can be obtained as second, third, and fourth harmonics, respectively.

Continuum, Inc. ND6000 dye laser pumped by a Surelite II Nd:YAG laser was used for the methylglyoxal experiment. The wavelengths of 812, 612, and 306 nm were obtained as the fundamental or frequency-doubled output.

Laser beam enters the instrument with horizontal polarization through a Brewster window in the detection region. It crosses the ion beam at  $90^\circ$  with interaction point being on the axis of symmetry of the velocity map imaging assembly.

## 2.5 Velocity map imaging assembly

Velocity map imaging [23] assembly is a device, consisting of a position-sensitive ion detector and an electrostatic lens, designed to image electrons preserving information about their initial velocity distribution. It maps all electrons with the same initial velocity to the same spot on the detector regardless of their initial position. The assembly operates in a pulsed mode so as not to interrupt the laser-ion interaction.

The electrostatic lens consists of three ring electrodes: top, middle, and bottom. The laser-

ion interaction takes place between middle and bottom electrodes. The bottom electrode has negative potential  $V_R$  and acts as a repeller electrode. The top electrode has positive potential  $V_E$  and acts as an extraction electrode. The optimal ratio of  $V_E/V_R$  necessary for velocity mapping is obtained by varying  $V_E/V_R$  around the value of 1.91 predicted by an ion-optics simulation software Simion [24]. The size of a photoelectron image is inversely proportional to  $V_R$ . Typical values for  $V_R$  are -200 V and -300 V.

The position-sensitive detector consists of two imaging-quality microchannel plates and a P43 phosphor screen. After leaving the region of electrostatic lens the detached electrons are further accelerated toward the front of the first microchannel plate, held at 2 kV. The amplified electrons from the first microchannel plate are accelerated toward the second microchannel plate, the back of which is held at 4 kV. Finally, the electrons exiting the second microchannel plate are accelerated toward a phosphor screen held at 6.5 kV. The electron impact positions are recorded by a thermoelectrically cooled CCD camera (CoolSNAP Myo, Photometrics, Inc.). The voltage on the second microchannel plate is 4 kV for about 200 ns only. Outside this time interval the voltage is 3 kV and no electrons are imaged. The whole imaging assembly is inside  $\mu$ -metal cup to shield it from Earth's magnetic field.

The photoelectron image is a 2D projection of outgoing 3D electronic wave function. Since 3D wave has cylindrical symmetry with respect to the axis of polarization, it is described uniquely by its cross section along this axis. The cross section is obtained from the 2D image using the inverse Abel transformation [25] implemented in the BASEX software [26]. Integrating over the

polar angle gives the radial distribution  $f(r)$ . Since

$$r \propto v \propto \sqrt{eKE},$$

the electron kinetic energy  $eKE$  distribution is obtained from  $f(r)$  using a Jacobian transformation:

$$g(eKE) = f(r) \frac{dr}{d(eKE)} \propto \frac{f(\sqrt{eKE})}{\sqrt{eKE}}.$$

The constant of proportionality is obtained by calibrating with well-known electron affinity of atomic oxygen [27, 28]. The electron binding energy  $eBE$  distribution is obtained from  $eKE$  distribution using the relation

$$eBE = h\nu - eKE.$$

## Chapter 3

# Methylglyoxal

Methylglyoxal (MG),  $\text{OHCC}(\text{CH}_3)\text{O}$ , along with other small dicarbonyls such as glyoxal (G) and biacetyl, is a minor component of Earth's atmosphere with significant contributions to the chemistry of volatile organic compounds [29–33]. In particular, irreversible reactions of dicarbonyls with  $\text{NH}_3/\text{NH}_4^+$  in cloud droplets lead to formation of "brown carbon", a subclass of light absorbing atmospheric aerosols [34].

Despite the relative importance and rather elementary structure of MG, no attempts to measure its electron affinity have been reported to date. In 1980, Rawlings and Davidson estimated the EA of MG theoretically [35]. Specifically, they obtained a restricted Hartree-Fock estimate of  $\text{EA} \sim 0.9 \text{ eV}$  for unsubstituted G. Then, based on the comparison to similar methyl-group substitutions, they proposed that  $\text{EA}(\text{MG})$  should be  $\sim 0.2 \text{ eV}$  lower than the above  $\text{EA}(\text{G})$  value, thus arriving at an estimate of  $\text{EA}(\text{MG}) \sim 0.7 \text{ eV}$ . Our work provides first robust experimental deter-

mination of the  $EA(MG) = 0.87(1)$  eV. It is interesting to note that Rawlings and Davidson's assertion (guided largely by chemical intuition) that  $EA(MG)$  should be  $\sim 0.2$  eV lower than  $EA(G)$  proved to be on target, even though their individual  $EA(G)$  and  $EA(MG)$  estimates both missed the mark. For comparison, recent work in the Sanov group provided a spectroscopic determination of  $EA(G) = 1.10(2)$  eV [16]. Hence,  $EA(MG) = 0.87(2)$  eV is indeed  $0.23(3)$  eV lower than  $EA(G)$ , in excellent agreement with Rawlings and Davidson's 0.2 eV prediction. However, since they underestimated  $EA(G)$  by 0.2 eV, their  $EA(MG)$  prediction suffered from a similar error.

The photochemistry and excited states of neutral MG have received more attention than its anion. Previous laser-induced phosphorescence and fluorescence studies have identified the lowest triplet state of MG adiabatically 2.414 eV above the ground state [36] and the lowest excited singlet adiabatically 2.743 eV above the ground state [37]. In this chapter, we compare these singlet-triplet and singlet-singlet splittings to the corresponding band intervals in the photoelectron spectrum of the MG anion.

In what follows, anion photoelectron imaging spectroscopy was used to probe the ground (closed-shell singlet  $X^1A'$ ) and two excited (lowest triplet  $a^3A''$  and open-shell singlet  $A^1A''$ ) electronic states of methylglyoxal, accessed from the corresponding radical anion,  $MG^- (X^2A'')$ . The experimental results are supported by *ab initio* calculations and Franck-Condon simulations and provide insight into the electronic structure of methylglyoxal, in both neutral and anion states.

### 3.1 Experimental results

In Figure 3.1, we present photoelectron spectra of MG anion obtained at 306 nm, 612 nm, and 812 nm laser wavelengths. We also show photoelectron spectrum of G obtained at 532 nm laser wavelength for comparison.

In the 306 nm spectrum of MG we identify three bands labeled A, B, and C. The band A is broad and congested, whereas the bands B and C are narrower and slightly more resolved. Every band corresponds to a transition from the ground state  $X^2A''$  of the MG anion to some electronic state of the neutral MG. We assign the bands A, B, and C to the singlet ground state  $X^1A'$ , the lowest triplet state  $a^3A''$ , and the first excited singlet state  $A^1A''$  of the neutral MG, respectively.

The origins of the bands correspond to adiabatic detachment energies or electron affinities (EAs) of corresponding states of neutral MG, whereas the band maxima correspond to vertical detachment energies (VDEs). The 812 nm MG spectrum reveals the origin of band A, the partially resolved peak at the beginning of the band. The maximum of this peak corresponds to  $EA(X^1A') = 0.87(1)$  eV. The maximum of band A in the 612 nm MG spectrum corresponds to  $VDE(X^1A') = 1.20(4)$  eV. The maximum of the first peak of band B corresponds to

$$EA(a^3A'') = VDE(a^3A'') = 3.27(2) \text{ eV}.$$

Similarly, the maximum of band C corresponds to

$$EA(A^1A'') = VDE(A^1A'') = 3.614(9) \text{ eV}$$

It is worth noting that single-triplet excitation energy  $EA(a^3A'') - EA(X^1A') = 2.40(3)$  eV obtained from our measurements perfectly matches the value 2.414 eV previously measured using phosphorescence spectroscopy [36]. Furthermore, the energy gap between the ground and first excited singlet states  $EA(A^1A'') - EA(X^1A') = 2.74(1)$  eV also perfectly matches the value 2.74 eV previously measured using fluorescence excitation spectroscopy [37]. In addition to these experimental confirmations, we performed *ab initio* calculations (See Tables 3.1 and 3.2) and Franck-Condon simulation of band B (See Figure 3.4) to support the assignments.

## 3.2 Theory vs Experiment: structures

We performed geometry optimization for the ground state  $X^2A''$  of MG anion, the ground state  $X^1A'$  and the lowest triplet state  $a^3A''$  of the neutral MG on Q-CHEM software using CCSD method with aug-cc-pVTZ basis set. We show the optimized minimum-energy structures in Figure 3.2 and summarize the geometric parameters defining them and the corresponding energies in Table 3.1. The structures of the ground state of MG anion and the lowest triplet state of neutral MG are visually identical, the structure of the ground state of neutral MG being visually distinct from them only by 60° rotation of the methyl group. In terms of quantitative distinctions, the ground state structure of MG anion has 6.6% shorter C1-C2 bond and about 5% longer C1-O1 and C2-O2 bonds than the ground state structure of neutral MG. In addition, both O1-C1-C2 and O2-C2-C1 angles are larger in the anion than in the neutral. So O1 gets farther from, and O2 closer to, the methyl group in the anion than in the neutral. This correlates with the

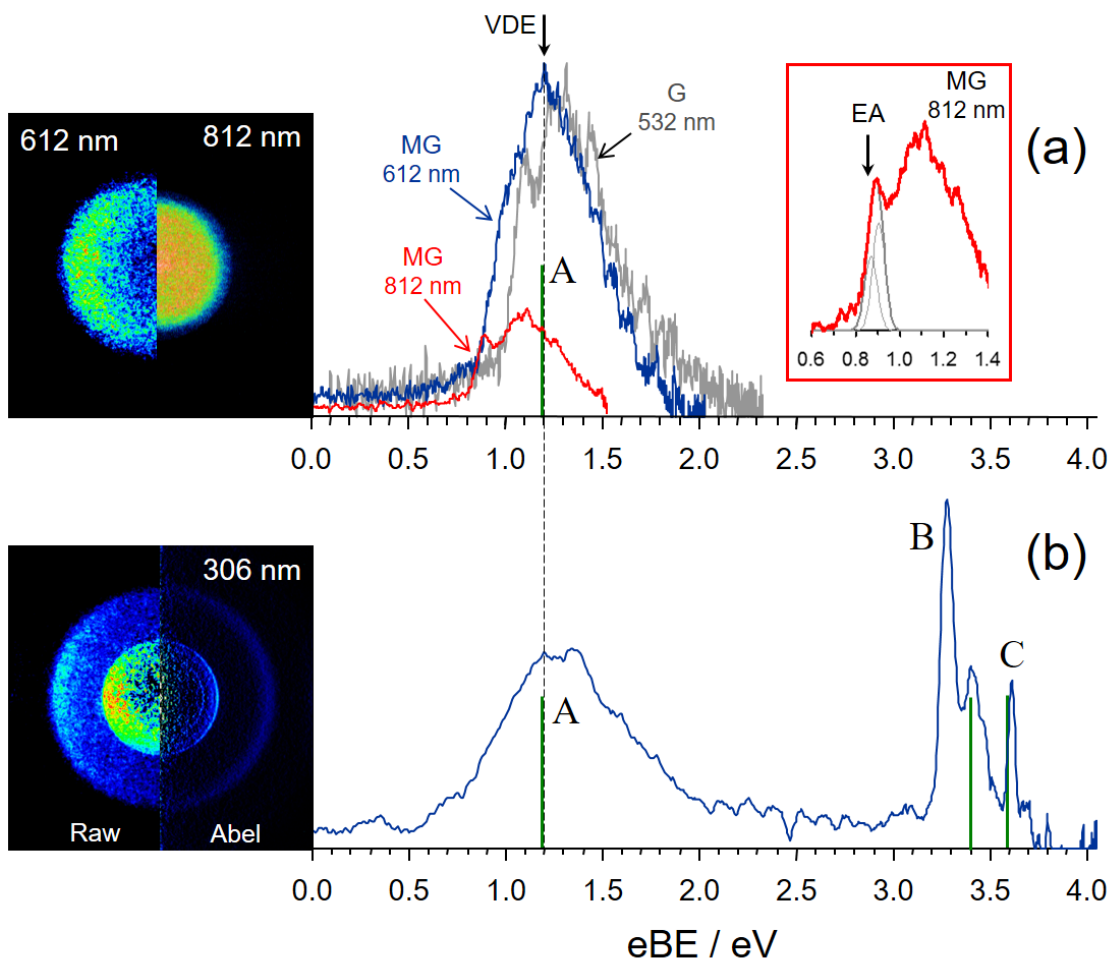


Figure 3.1: Anion photoelectron images and spectra of methylglyoxal (MG). (a) Composite of the unprocessed 612 nm and 812 nm MG images (left and right halves, respectively) and the corresponding spectra shown in red and blue, as indicated. The 532 nm anion photoelectron spectrum of unsubstituted glyoxal (G) is also included for comparison (in gray). The inset shows the magnified portion of the 812 nm MG spectrum, with the vertical arrow indicating the adiabatic electron affinity,  $EA = 0.87(1)$  eV. (b) The composite 306 nm anion photoelectron image of MG, consisting of raw (left) and Abel-inverted (right) data, and the corresponding photoelectron spectrum. Band A in all spectra is assigned to the singlet ground state of the neutral molecule. Band B is assigned to the lowest-lying triplet state of MG and band C to the first excited singlet. The green vertical bars in (a) and (b) indicate the VDEs, calculated at the EOM-IP-CCSD/aug-cc-pVTZ level of theory. See Table 3.2 and the text for details.

orientation of the methyl group that maximizes the interaction of hydrogen atoms with O1 in the neutral and O2 in the anion. The lowest triplet state structure of neutral MG is distinct from the ground state structure of neutral MG in a similar manner, but the differences are less pronounced (for example, the triplet structure has 3% shorter C1-C2 bond than the ground state structure of neutral MG).

The difference or similarity of the structures explain the shapes of the bands. According to the Franck-Condon principle the larger the difference between the equilibrium geometries of the initial and final states of a transition the broader is the corresponding band. Band A is almost three times as broad as band B. This is consistent with the fact that the anion structure is more similar to the structure of the triplet than to the structure of the ground state of the neutral. It is important to note that the broadness of band A cannot be attributed to 60° rotation of the methyl group, even though it is the most apparent visual distinction. This follows from the fact that the 532 nm spectrum of G is as broad as the 612 nm spectrum of MG (See Figure 3.1).

In Table 3.2 we present nominal electron configurations for all the states under consideration. The same nature of the changes in the anion and triplet structures, relative to the ground state structure of the neutral, indicate the special role played by  $4a''$  molecular orbital (MO). In Figure 3.3, we show the HOMO  $4a''\alpha$  and HOMO-1  $16a'\alpha$  of MG anion. They also provide qualitative descriptions of corresponding MOs of the lowest triplet and ground states of the neutral.  $4a''$  MO has strong bonding character with respect to C1-C2 bond and antibonding character with respect to C1-O1 and C2-O2 bonds. This explains the shortening of C1-C2 bond and lengthening of C1-O1 and C2-O2 bonds in the anion and triplet structures due to population of  $4a''$

MO.

### 3.3 Theory vs Experiment: energies

Energies (without zero-point corrections) corresponding to structures obtained using CCSD method with aug-cc-pVTZ basis set are shown in Table 3.1. We also show the energies of neutral states relative to the anion ground state energy, labeled as  $\Delta E$ -CCSD energies. These are estimations of adiabatic detachment energies or EAs of corresponding states.  $\Delta E$ -CCSD approach underestimates experimental  $EA(X^1A')$  by 0.11 eV and overestimates experimental  $EA(a^3A'')$  by 0.23 eV. The deviation from the experiment for the excited state is expectedly larger.

We also used  $\Delta E$ -CCSD approach to estimate  $VDE(X^1A')$  and  $VDE(a^3A'')$ . Specifically, we performed single-point energy calculations for  $X^1A'$  and  $a^3A''$  states at the ground state equilibrium geometry of MG anion. VDEs correspond to these energies expressed relative to the ground state energy of MG anion. We present the results in Table 3.2. For state  $X^1A'$  the agreement between the theory and the experiment is excellent, the calculation overestimating experimental  $VDE(X^1A')$  by about 0.05 eV. For state  $a^3A''$  the calculation overestimates experimental  $VDE(a^3A'')$  by about 0.29 eV. It should be noted that the theoretical  $VDE(a^3A'')$  is very close to the theoretical  $EA(a^3A'')$ , the difference being about only 0.06 eV. This supports our assignment of experimental  $VDE(a^3A'')$  and  $EA(a^3A'')$  to the same value of 3.27(2) eV corresponding to the maximum of the first peak in band B in Figure 3.1. Similar to EA calculations,  $\Delta E$ -CCSD approach expectedly gives more accurate VDE for the ground state.

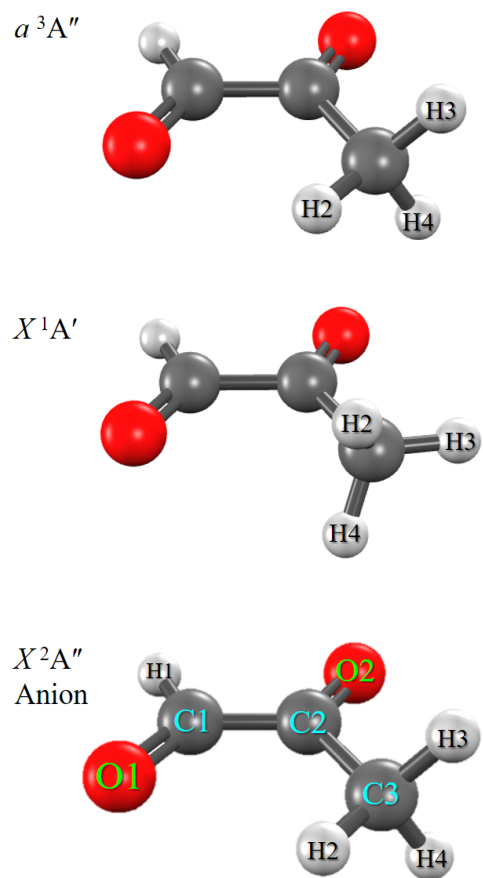


Figure 3.2: The optimized minimum-energy structures of the MG anion ( $X^2A''$ ) and the neutral in the  $X^1A'$  and  $a^3A''$  electronic states. The corresponding geometric parameters are reported in Table 3.1.

Table 3.1: Geometric parameters defining the equilibrium geometries of the methylglyoxal anion in the  $X^2A''$  state and the neutral methylglyoxal molecule in the  $X^1A'$  and  $a^3A''$  states, represented pictorially in Figure 3.2. The structures were optimized using CCSD/aug-cc-pVTZ. The bond lengths are in Angstroms, while the angles are in degrees. Bold emphasis: neutral parameters exhibiting significant deviations from the anion geometry (at least 0.05 Å or 3°). Electronic energies relative to the anion structure (i.e., the adiabatic electron affinities) are also given and compared to the experimental values.

Parameter	Anion $X^2A''$	$X^1A'$	$a^3A''$
C1-C2	1.4205	<b>1.5208</b>	<b>1.4765</b>
C1-O1	1.2630	<b>1.2000</b>	1.2318
C1-H1	1.1004	1.0961	1.0843
C2-O2	1.2620	<b>1.2050</b>	1.2218
C2-C3	1.5099	1.4924	1.5031
C3-H2	1.0880	1.0883	1.0872
C3-H3	1.0920	1.0841	1.0873
O1-C1-C2	126.94	<b>122.90</b>	<b>122.51</b>
H1-C1-C2	113.00	113.78	114.45
O2-C2-C1	123.00	<b>117.57</b>	121.33
C3-C2-C1	117.79	117.24	116.31
H2-C3-H3	109.60	110.52	110.62
H3-C3-H4	107.33	110.52	108.69
H2-C3-H4	109.60	106.82	110.62
C2-C3-H2	110.89	109.56	108.32
C2-C3-H3	109.67	109.81	109.28
C1-C2-C3-H2	0	<b>-58.44</b>	0
C1-C2-C3-H3	-121.19	<b>180</b>	-120.59
CCSD energy/Hartree	266.830680	266.802790	266.701914
$\Delta E$ -CCSD energy/eV (relative to anion)	0	0.759	3.504
Experimental EA/eV		0.87(1)	3.27(2)

By its very nature,  $\Delta E$ -CCSD approach does not treat an anion and a neutral on an equal footing when calculating EAs or VDEs. Specifically, the approach uses different reference wavefunctions for the anion and the neutral. In order to resolve this exact problem we calculated VDEs using three different equation-of-motion coupled-cluster methods: "electron affinity" (EOM-EA-CCSD), "ionization potential" (EOM-IP-CCSD and EOM-IP-CCSD(dT)), and "spin-flip" (EOM-SF-CCSD). These are single-point calculations using aug-cc-pVDZ basis set and CCSD/aug-cc-pVTZ optimized geometry of MG anion described above (See Table 3.1 and Figure 3.2). We present the results in Table 3.2.

EOM-EA-CCSD method was used to calculate  $VDE(X^1A')$  adding an electron to the neutral reference wavefunction corresponding to  $X^1A'$ . EOM-IP-CCSD and EOM-IP-CCSD(dT) methods were used to calculate  $VDE(X^1A')$ ,  $VDE(a^3A'')$ , and  $VDE(A^1A'')$  removing either an  $\alpha$  or a  $\beta$  electron from the anion reference wavefunction corresponding to  $X^2A''$ . EOM-SF-CCSD method was used to calculate singlet-triplet vertical gaps between neutral MG states  $X^1A'$ ,  $a^3A''$ , and  $A^1A''$ . Then these energies were combined with EOM-IP-CCSD(dT)  $VDE(a^3A'')$  to yield  $VDE(X^1A')$  and  $VDE(A^1A'')$ . EOM-IP-CCSD(dT) method produced the most accurate results. We show them in Figure 3.1 as green vertical bars. For states  $X^1A'$  and  $A^1A''$  the difference between theory and experiment is on the order of 0.01 eV. Whereas for state  $a^3A''$  the differences are about 0.1 eV.

Table 3.2: Properties of the anion and neutral MG states at the CCSD/aug-cc-pVTZ optimized geometry of the anion, determined using the methods indicated. All calculations used the aug-cc-pVTZ basis set. See the text for details. The computed results are compared to the corresponding experimental band positions (from Figure 3.1). Bold values indicate the recommended (highest-level) theory predictions.

MG state	Electron configuration	Relative energy / eV		
		Vertical	Adiabatic	Method
$X^2A''$ (anion)	$\dots(3a'')^2(16a')^2(4a'')^1$			
$X^1A'$	$\dots(3a'')^2(16a')^2(4a'')^0$	1.249	0.759	$\Delta E$ -CCSD
		1.149		EOM-EA-CCSD
		1.271		EOM-IP-CCSD
		<b>1.192</b>		<b>EOM-IP-CCSD(dT)</b>
		1.249 <sup>a</sup>		EOM-IP-CCSD(dT)/SF-CCSD
		1.20(4)	0.87(1)	Experiment (band A)
$a^3A''$	$\dots(3a'')^2(16a')^1(4a'')^1$	3.566	3.504	$\Delta E$ -CCSD
		3.467		EOM-IP-CCSD
		<b>3.396</b>		<b>EOM-IP-CCSD(dT)</b>
			3.27(2) <sup>b</sup>	Experiment (band B)
$A^2A''$	$\dots(3a'')^2(16a')^1(4a'')^1$	3.685		EOM-IP-CCSD
		<b>3.580</b>		<b>EOM-IP-CCSD(dT)</b>
		3.713 <sup>c</sup>		EOM-IP-CCSD(dT)/SF-CCSD
			3.614(9) <sup>b</sup>	Experiment (band C)

<sup>a</sup> Obtained by subtracting the 2.047 eV singlet-triplet vertical energy gap (at the anion geometry), calculated using EOM-SF-CCSD, from the VDE = 3.396 eV corresponding to the triplet state, calculated using EOM-IP-CCSD(dT).

<sup>b</sup> Narrow peak maxima assumed to represent both the adiabatic and vertical energy gaps between the anion and neutral states of similar equilibrium geometries.

<sup>c</sup> Obtained by adding the 0.317 eV vertical energy gap between the  $a^3A''$  and  $A^1A''$  states (at the anion geometry), calculated using EOM-SF-CCSD, to the VDE = 3.396 eV corresponding to the  $a^3A''$  state, calculated using EOM-IP-CCSD(dT).

### 3.4 Theory vs Experiment: Franck-Condon simulation

In Figure 3.4 we show the Franck-Condon (FC) simulation of band B. The result in red perfectly matches the profile of band B and clearly shows that band C is not a part of it, but corresponds to a different electronic transition. FC intensities were obtained on the PESCAL program [38] using CCSD/aug-cc-pVTZ geometries of MG anion  $X^2A''$  and neutral triplet  $a^3A''$ , for logistic reasons, obtained on Gaussian instead of Q-CHEM. The stick spectrum in Figure 3.4 corresponds to these intensities multiplied by an  $eKE^{3/2}$  pre-factor, accounting for the Wigner-like scaling of the electronic part of the photodetachment cross section near zero  $eKE$  [39]. The smooth FC profile in red was obtained by convoluting the stick spectrum in the speed domain with an instrumental resolution function, taken to be a Gaussian with  $FWHM = 2 \times 10^4$  m/s determined from  $O^-$  photodetachment under similar experimental conditions. The only fitting procedure was shifting the FC profile along the energy axis to match the first peak of band B. As a result, we obtain adiabatic EA of the lowest triplet state  $a^3A''$  of neutral MG given by the 0-0 transition energy = 3.27 eV.

### 3.5 Summary

We characterized the three lowest electronic states of neutral MG, the singlet ground state  $X^1A'$ , the lowest triplet state  $a^3A''$ , and the open-shell singlet state  $A^1A''$ , accessed from its anion  $MG^-$  in the ground state  $X^2A''$  using negative-ion photoelectron imaging spectroscopy. In particular,

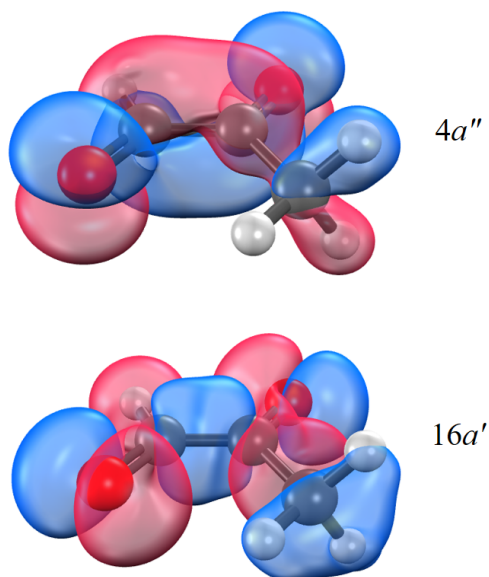


Figure 3.3: The  $16a' - \alpha$  (HOMO - 1) and the  $4a'' - \alpha$  HOMO of the MG anion from CCSD/aug-cc-pVTZ calculations.

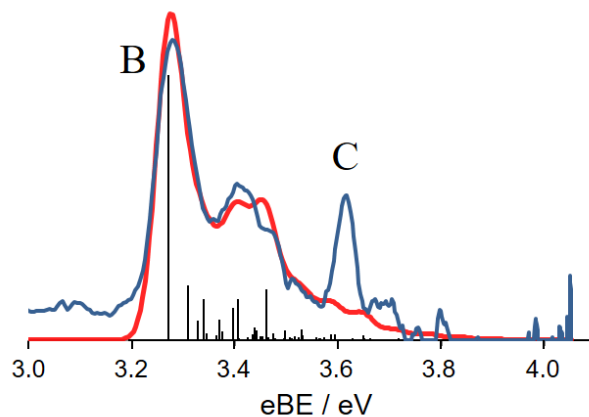


Figure 3.4: The blue line is a magnified portion of the 306 nm anion photoelectron spectrum of methylglyoxal reproduced from Figure 3.1. The results of the Franck-Condon simulation for the triplet transitions are shown in black as discrete transitions, while the red spectrum is the simulation convoluted with a Gaussian function representing instrument resolution. See the text for details.

the EA of MG was measured for the first time. The experimental results were supported by high-level *ab initio* geometry optimization calculations for all states except the open-shell singlet, and the Franck-Condon simulation of the band corresponding to the triplet state. The agreement between the experiment and theory is perfect. Furthermore, the experimental singlet-singlet and singlet-triplet gaps were consistent with the past fluorescence [37] and phosphorescence [36] measurements.

The equilibrium geometries of the ground states of the neutral MG and its anion are visually identical, with the exception of the orientation of the methyl group. However, the difference in the orientation of the methyl group is not responsible for the broadness of band A. The main distinction between the geometries is the length of the central C-C bond, which is shorter in the anion. The equilibrium geometries of the ground state of MG anion and the lowest triplet state of neutral MG are very similar, which explains the sharpness of the band B.

The Franck-Condon simulation of band B perfectly matched the profile of the band, confirming that band C corresponds to the open-shell singlet state. We did not perform the geometry optimization for the open-shell singlet, but based on the sharpness of band C we expect its equilibrium geometry to be similar to the one of MG anion.

## Chapter 4

### Biacetyl and its cluster anions

Biacetyl (BA) is the common name of dimethylglyoxal. Together with singly substituted methylglyoxal (MG) and unsubstituted glyoxal (G), BA is a member of the family of small dicarbonyls with important roles in atmospheric chemistry [40–42]. It is a volatile organic compound, relatively abundant in the atmosphere. Its oxidation in the presence of nitric oxide leads to the formation of ozone and other important processes [43].

Surprisingly little is known about this relatively simple yet important molecule, especially concerning its photochemistry, oligomerization (cluster formation), and interactions with electrons and ions. The adiabatic electron affinity of BA was determined previously to be 0.69(1) eV using an indirect temperature dependent equilibrium ion/molecule reaction method [44]. The electron binding and other properties of BA oligomers, however, have remained largely unknown. The most recent study of BA oligomers was the 1938 work by Molds and Riley investigating the

polymerization of MG and BA [45]. They reported that MG undergoes polymerization with mass loss, and the rate of the process increases with the addition of water, while BA was not found to polymerize under the same conditions.

In this chapter we present our original spectroscopic investigation of BA and its cluster anions. A typical cluster anion consists of a charged core, holding the excess electron, and surrounding neutral solvent molecules. So a typical cluster anion is mainly held together by charge-dipole/induced dipole interactions. However, as our study shows, this is not the case for cluster anions of biacetyl,  $\text{BA}_{n=2,3,4}^-$ , where the excess electron is delocalized over the whole cluster. In other words, the cluster is held together by weakly covalent interactions. We explore the nature of these interactions. In particular, we gauge their strength and extent of charge delocalization. The analysis is based on photoelectron spectra of  $\text{BA}_{n=2,3,4}^-$ , and is supported by high level ab initio and DFT calculations.

## 4.1 Experimental results: biacetyl anion

In Figure 4.1, we show the photoelectron spectrum and image of biacetyl (BA) anion obtained at 355 nm laser wavelength. For comparison, we also show photoelectron spectrum of MG anion obtained at 306 nm laser wavelength [16]. Expectedly, the spectra of BA and MG have very similar profiles, the former being slightly shifted to the left with respect to the latter. Just like in the case of G and MG (See Figure 3.1), the shift is attributed to the destabilizing effect of additional methyl group in BA.

The spectrum of BA consists of two bands labeled A and B. Just like for MG, we assign bands A and B to the electronic transitions from the ground state  $X^2A_u$  of  $BA^-$  to the ground state  $X^1A_g$  and the lowest triplet state  $a^3A_u$  of neutral BA. The band C in the MG spectrum is not present in the BA spectrum, but it is expected to appear in BA spectra obtained at higher photon energy.

The origins of the bands correspond to adiabatic detachment energies or electron affinities (EA) of corresponding states of neutral BA, whereas the band maxima correspond to vertical detachment energies (VDE). So the maxima of bands A and B correspond to  $VDE(X^1A_g) = 1.12(5)$  eV and  $VDE(a^3A_u) = 3.05(5)$  eV, respectively. The onset of band B corresponds to  $EA(a^3A_u) = 3.05(5)$  eV. The origin of band A is poorly defined and gives only an estimate  $EA(X^1A_g) < 0.7$  eV. We included these values in Table 4.2 for comparison with the results of calculations.

## 4.2 Experimental results: cluster anions of biacetyl

In Figure 4.2(a), we show the photoelectron spectra of  $BA^-$ ,  $BA^- \cdot N_2O$ ,  $BA^- \cdot H_2O$ , and  $(BA)_2^-$  obtained at 532 nm laser wavelength. The spectrum of  $BA^-$  contains a single broad congested band corresponding to band A in the 355 nm spectrum of  $BA^-$  (See Figure 4.1). As discussed in Section 4.1, we assigned this band to the electronic transition from the ground state  $X^2A_u$  of  $BA^-$  to the ground state  $X^1A_g$  of neutral BA. The spectra of  $BA^- \cdot N_2O$  and  $BA^- \cdot H_2O$  are expectedly almost identical to the spectrum of  $BA^-$ , but shifted to the higher binding energies. The relatively weak solvation interaction stabilizes the core anion increasing the binding energy of an excess electron, yet not disturbing its electronic structure much. The ion-dipole interaction

between  $\text{BA}^-$  and very polar water molecule is much stronger than the ion-induced dipole interaction between  $\text{BA}^-$  and almost nonpolar  $\text{N}_2\text{O}$ . Hence, the shift (0.44 eV) for  $\text{BA}^- \cdot \text{H}_2\text{O}$  is larger than the shift (0.14 eV) for  $\text{BA}^- \cdot \text{N}_2\text{O}$ . The shifts correspond to solvation energies and were quantified by maximizing the overlap between the corresponding bands as shown in Figure 4.2(b).

The 532 nm spectrum of  $(\text{BA})_2^-$  contains two bands: the broad congested lower-energy band resembling the band present in the spectrum of  $\text{BA}^-$  and the sharp band at the high-energy end of the spectrum. There are two important points to note. The first point is that the shift (0.59 eV) for  $(\text{BA})_2^-$  is larger than the shift (0.44 eV) for  $\text{BA}^- \cdot \text{H}_2\text{O}$ , even though BA is nonpolar. In other words, the shift cannot be accounted for by typical solvation interaction between  $\text{BA}^-$  and BA. The second point is that the sharp band does not have a corresponding band in the spectrum of  $\text{BA}^-$ . In other words, the origin of the sharp band cannot be attributed to the electronic structure of isolated  $\text{BA}^-$ . We will discuss the origin of the sharp band in more detail later. For now we note that both points strongly indicate that the intermolecular interaction in  $(\text{BA})_2^-$  is of covalent nature, which motivated us to study larger cluster anions of BA in more detail.

In Figure 4.3(a), we show the photoelectron spectra of  $\text{BA}^-$  and its cluster anions  $(\text{BA})_{n=2-4}^-$  obtained at 355 nm laser wavelength. The spectra of all the cluster anions contain a broad congested band present in the spectrum of  $\text{BA}^-$  described in Section 4.1. Notably the spectrum of  $(\text{BA})_2^-$  no longer has a sharp band that is present in the 532 nm spectrum of  $(\text{BA})_2^-$  around 2.3 eV. Instead there is a similar sharp band of lower intensity at the high-energy end of the spectrum. Hence, these bands cannot be due to direct photodetachment to any specific state of neutral

BA, as such transition would appear at the same eBE, independent of the laser wavelength. Considering the fact that these bands correspond to electrons with almost zero KE, they are likely due to autodetachment from excited states of  $(\text{BA})_2^-$ . The similar autodetachment bands are also present in the spectra of the other cluster anions  $(\text{BA})_{n=3,4}^-$ . The absence of such an autodetachment band in the spectrum of  $\text{BA}^-$  strongly suggests that the excited anionic state responsible for the autodetachment is of intermolecular nature, that is, it requires electron delocalization between at least two BA molecules. In other words, the intermolecular interactions in cluster anions  $(\text{BA})_{n=2-4}^-$  have covalent character, which is in line with our previous analysis of the 532 nm spectrum of  $(\text{BA})_2^-$ .

## 4.3 Theory vs Experiment: biacetyl anion

### 4.3.1 Structures

In Figure 4.4, we show structures of the ground state  $X^2A_u$  of  $\text{BA}^-$ , the singlet ground state  $X^1A_g$  and the lowest triplet state  $a^3A_u$  of neutral BA, optimized at the CCSD/aug-cc-pVDZ level of theory on Q-CHEM [46]. These calculations were preceded by preliminary DFT calculations at the M06-2X/aug-cc-pVDZ level of theory. We show the corresponding geometric parameters in Table 4.1. All three structures belong to the  $C_{2h}$  symmetry point group, with all heavy atoms located in the same plane. Visually, the structures of the triplet neutral and the anion are indistinguishable, whereas the structure of the singlet neutral is distinct from them only in the

orientation of methyl groups. Quantitatively, attaching an electron to neutral BA shortens C2-C3 bond by about 6.7% and lengthens C2-O1 and C3-O2 bonds by about 5%. In addition, in the anion the oxygens are closer to the adjacent methyl groups than in the singlet neutral, which correlates with the orientations of methyl groups that maximize the interaction between hydrogens and oxygens. The structure of the triplet neutral is distinct from the structure of the singlet neutral in a similar manner, but the differences are less pronounced (for example, the structure of the triplet neutral has 4% shorter C2-C3 bond than the structure of the singlet neutral). It should be noted that we observed almost the same patterns for MG discussed in Chapter 3.

Just as for  $MG^-$ , the broadness of Band A in the 355 nm spectrum of  $BA^-$  is attributed to the difference between the equilibrium structures of the ground state  $X^2A_u$  of  $BA^-$  and the singlet ground state  $X^1A_g$  of neutral BA, according to the Franck-Condon principle. Similarly, the sharpness of Band B in the 355 nm spectrum of  $BA^-$  is attributed to the similarity of the equilibrium structures of the ground state  $X^2A_u$  of  $BA^-$  and the lowest triplet state  $a^3A_u$  of neutral BA. Considering the fact that the band in the 532 nm spectrum of glyoxal (See Figure 3.1) is as broad as band A in the 355 nm spectrum of BA, it is important to note that the broadness of band A is not due to 60° rotation of the methyl group, even though it is the most apparent visual distinction.

Despite not being spectroscopically important, the orientation of the methyl groups plays an interesting role in interpreting the structures of cluster anions of BA. Therefore, we are going to refer to structures of BA as adopting "neutral" (*nu*) or "anion" (*an*) structural motifs depending on the orientation of methyl groups. For example, the triplet neutral adopts *an* structural motif.

We verified that the structures obtained with CCSD/aug-cc-pVDZ approach are true potential minima by performing DFT (M06-2X/aug-cc-pVDZ) calculations which showed that there are no imaginary vibrational frequencies for these structures. Whereas, the same DFT calculations showed that  $C_{2h}$  (*an*) structure of the singlet neutral has two imaginary frequencies and lies 0.086 eV higher than the true potential minimum. Similarly,  $C_{2h}$  (*nu*) structures of the anion and the triplet neutral each indicated two imaginary frequencies and were found to be 0.028 eV (anion) and 0.034 eV (triplet) higher than the respective potential minima.

### 4.3.2 Energies

In Table 4.2, we show adiabatic (electron affinities (EAs)) and vertical detachment energies (VDEs) for the ground state  $X^1A_g$  and the lowest triplet state  $a^3A_u$  of neutral BA, obtained at different levels of theory. In M06-2X and CCSD approaches, EAs are calculated by subtracting the ground state energy of  $BA^-$  from the equilibrium energy of the corresponding state of neutral BA. Experimentally, EAs correspond to the origin of bands. Since the origin of band A is poorly defined, there is only an upper bound of 0.7 eV for  $EA(X^1A_g)$ . The CCSD value for  $EA(X^1A_g)$  is consistent with this estimation being  $\approx 0.15$  eV below this upper bound. Whereas, the M06-2X value for  $EA(X^1A_g)$  is 0.1 eV above this upper bound. For  $EA(a^3A_u)$ , both CCSD and M06-2X methods surprisingly give almost the same results, difference between them being only 0.02 eV. Both values overestimate the experimental  $EA(a^3A_u)$  by about 0.2 eV.

In M06-2X and CCSD approaches, VDEs are calculated as positive differences between ener-

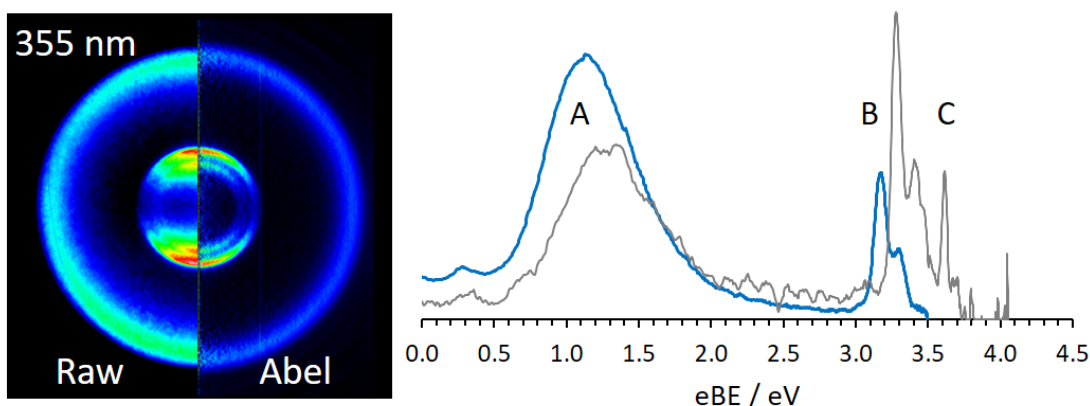


Figure 4.1: Left: a composite photoelectron image of BA anion obtained at 355 nm. The direction of the laser polarization is vertical in the image plane. The left half of the composite image represents the corresponding half of the raw experimental image, while the right half represents the corresponding Abel inversion. The corresponding photoelectron spectrum is shown to the right of the image (bold blue curve). It is compared to the previously reported photoelectron spectrum of methylglyoxal obtained at 306 nm (gray curve).

Table 4.1: Geometric parameters for the three  $C_{2h}$  symmetry structures<sup>a</sup> shown in Figure 4.4: the BA<sup>-</sup> anion ( $X^2A_u$  electronic state), the BA ground state singlet ( $X^1A_g$ ), and the lowest triplet ( $a^3A_u$ ).

parameter	anion	singlet	triplet
C2-C3	1.446	<b>1.550</b>	1.489
C1-C2	1.530	1.514	1.519
C2-O1	1.282	<b>1.222</b>	1.249
C1-H1	1.107	1.099	1.103
C1-H3	1.101	1.103	1.102
O1-C2-C3	123.9	<b>119.1</b>	120.8
O1-C2-C1	118.4	<b>124.1</b>	121.6
C2-C1-H1	109.4	109.2	109.5
C2-C1-H3	111.4	109.7	108.2
C3-C2-C1-H1	121.5	<b>180.0</b>	120.5
C3-C2-C1-H3	0.0	<b>58.5</b>	0.0

<sup>a</sup>All structures were optimized at the CCSD theory level using the aug-cc-pVDZ basis set. The numbering of the atoms is defined in Figure 4.4. The bond lengths are in Angstroms, and the angles are in degrees. Bold emphasis: neutral (singlet and triplet) parameters with the most significant deviations from the anion geometry (at least 0.05 Å or 4°).

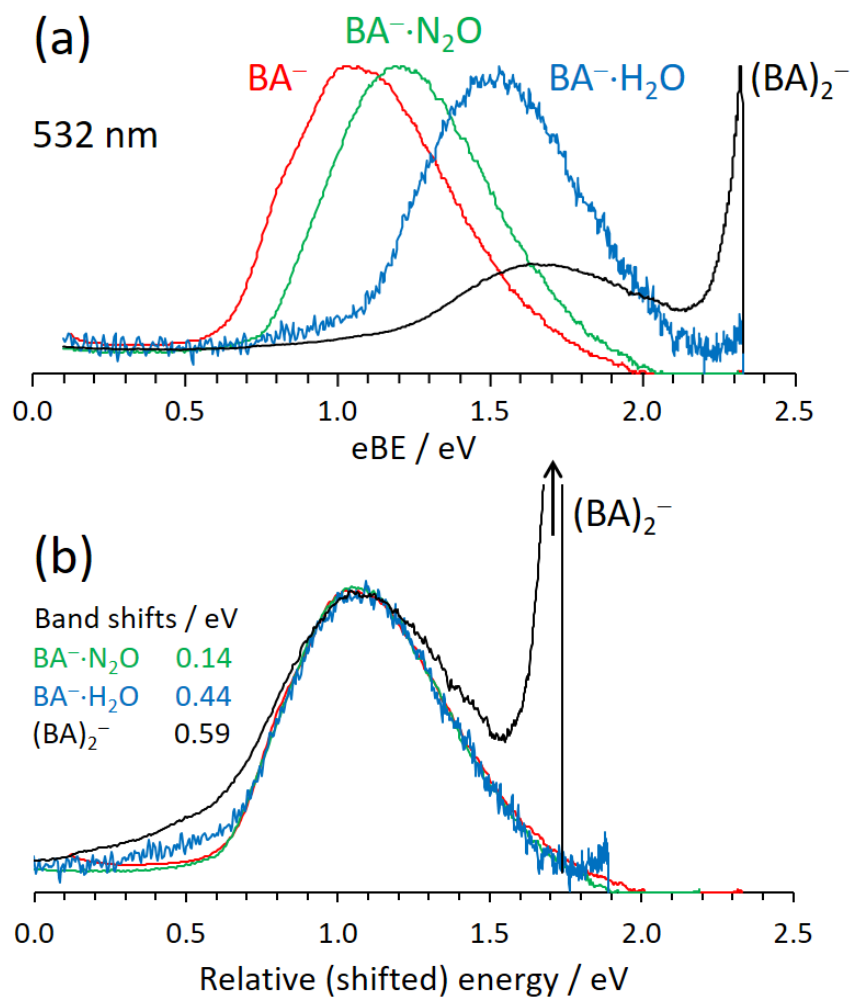


Figure 4.2: (a) Photoelectron spectra of BA<sup>-</sup> and its solvated clusters BA<sup>-</sup>·N<sub>2</sub>O and BA<sup>-</sup>·H<sub>2</sub>O, as well as the (BA)<sub>2</sub><sup>-</sup> dimer anion, obtained at 532 nm. (b) The same spectra as in (a) shifted back in energy for the best overlap with the BA<sup>-</sup> spectrum. The shifts are indicated in the figure. Their estimated uncertainty is ±0.01 eV.

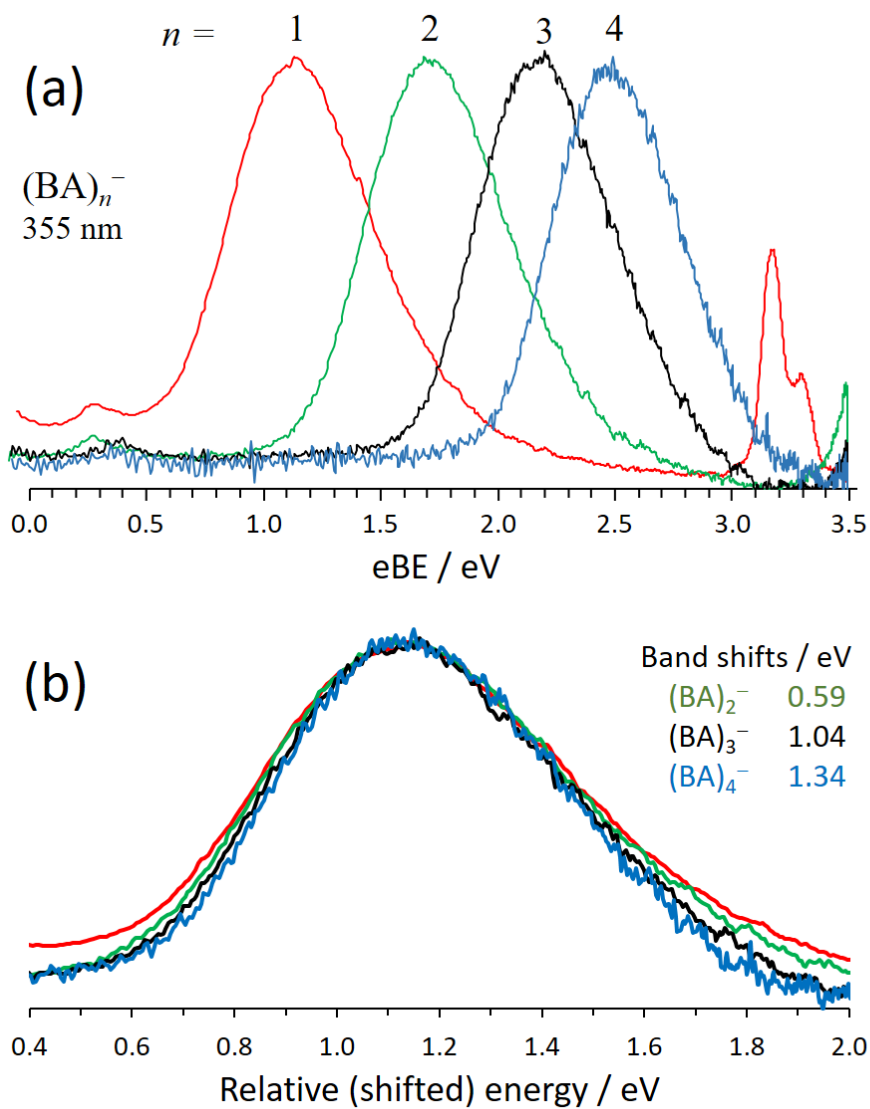


Figure 4.3: (a) Photoelectron spectra of  $(\text{BA})_n^-$ ,  $n = 1 - 4$  obtained at 355 nm. (b) The same spectra as in (a) shifted back in energy for the best overlap with the  $\text{BA}^-$  spectrum. The band shifts are indicated in the figure. Their estimated uncertainty is  $\pm 0.01$  eV.

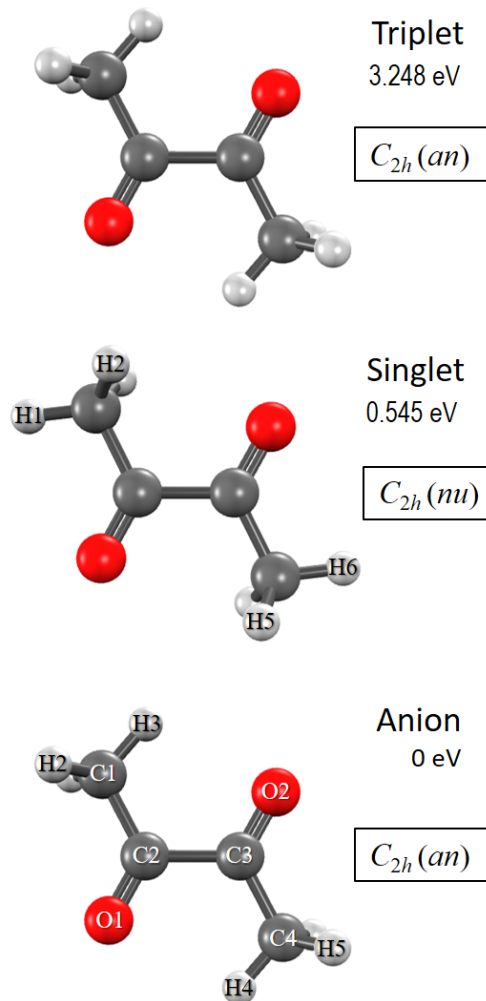


Figure 4.4: Bottom to top in order of increasing energy: BA anion ( $X^2A_u$ ), singlet ( $X^1A_g$ ), and triplet ( $a^3A_u$ ) structures optimized at the CCSD/aug-cc-pVDZ level of theory. The energies shown are adiabatic electronic energies relative to the anion equilibrium. Each of the three structures belongs to the  $C_{2h}$  symmetry point group, and all geometric parameters are given in Table 4.1. The torsional orientations of the methyl groups in the neutral singlet and anion structures define the respective “neutral” (nu) and “anion” (an) structural motifs. The nu and an designations refer to the geometric structures, not the charges (for example, the neutral triplet state adopts the an structural motif).

gies of the ground state of  $\text{BA}^-$  and the corresponding state of neutral BA both at the equilibrium geometry of  $\text{BA}^-$ . Experimentally, VDEs correspond to band maxima. The CCSD value for  $\text{VDE}(X^1A_g)$  is in excellent agreement with the experiment. The M06-2X value for  $\text{VDE}(X^1A_g)$  overestimates the experimental value by about 0.25 eV. For  $\text{VDE}(a^3A_u)$ , both CCSD and M06-2X methods give very close results, the difference between them being  $\approx 0.04$  eV, that overestimate the experimental value by  $\approx 0.2$  eV.

We also performed EOM-IP-CCSD calculations of VDEs. These are single point calculations at the CCSD/aug-cc-pVDZ optimized geometry. Unlike the previous approaches, EOM-IP-CCSD method describes the initial and final states using the same reference [47]. Since CCSD value for  $\text{VDE}(X^1A_g)$  is in excellent agreement with the experiment, the main improvement provided by EOM-IP-CCSD method is for  $\text{VDE}(a^3A_u)$ , the calculation result perfectly matching the experimental result. Considering the vertical singlet-triplet splitting

$$\Delta E_{S-T} = \text{VDE}(a^3A_u) - \text{VDE}(X^1A_g)$$

reveals even better performance of EOM-IP-CCSD method, which predicts the gap 2.077 eV perfectly matching the experimental result 2.05(5) eV. Whereas, CCSD overestimates the experimental value by more than 0.3 eV.

## 4.4 Theory vs Experiment: cluster anions of biacetyl

### 4.4.1 Structures

Several preliminary exploratory calculations starting from random initial geometries led to the structures of  $\text{BA}_2^-$  shown in Figure 4.5, optimized at the M06-2X/aug-cc-pVDZ level of theory with appropriate symmetry constraints. We took a DFT approach with M06-2X functional, chosen for its performance on delocalized systems with noncovalent interactions [48], because ab initio coupled cluster calculations became computationally too expensive at this level of complexity. The three structures are close in energy and correspond to potential minima as confirmed by vibrational frequency calculations. Each structure has sandwich-like appearance, two BA molecules situated parallel to each other and each adopting one of the *an* or *nu* structural motifs, distinguished by the torsional orientation of methyl groups as described in Subsection 4.3.1. As a result, each structure belongs to a particular symmetry point group motivating the labels:  $C_2$  (*an-nu*),  $D_2$  (*an-an*), and  $D_2$  (*nu-nu*). In every structure, the distance between BA molecules, defined as the distance between middle points of central C-C bonds, is about 3 Å. In contrast, the length of a typical covalent bond is 1-2 Å.

The fact that the most stable structure is  $C_2$  (*an-nu*) may suggest that in  $\text{BA}_2^-$ , as in a typical cluster anion, the excess charge is localized on one of BA molecules, the other BA molecule acting as a solvent. However, this picture is inconsistent with the experimental results as discussed in Section 4.2. Moreover, even according to calculations the excess charge is delocalized over the

whole cluster, the total Mulliken charges of the *an* and *nu* BA moieties in  $C_2$  (*an-nu*) structure being -0.52 and -0.48, respectively. In  $D_2$  (*an-an*) and  $D_2$  (*nu-nu*) structures, expectedly, the excess charge is equally distributed between BA molecules.

In Figure 4.7(b), we show the contour plot of HOMO of  $BA_2^-$  obtained at the M06-2X/aug-cc-pVDZ level of theory using  $C_2$  (*an-nu*) structure. The electron density around each BA molecule resembles very much HOMO of  $BA^-$  shown in Figure 4.7(a) and described in Subsection 4.3.1. Just like the HOMO of  $BA^-$ , the HOMO of  $BA_2^-$  has  $\pi$  bonding character along the central C-C bond and  $\pi^*$  antibonding character along C-O bonds of each BA molecule. However, in  $BA_2^-$ , the  $\pi$  lobes along central C-C bonds in each BA molecule are not isolated, but actually overlap creating an electron density between two BA molecules. Since, in the case of  $BA_2^-$ , the HOMO is occupied by a single electron, we can describe this  $\pi$ - $\pi$  interaction as an order-of-1/2 covalent bond between two BA molecules.

For larger cluster anions  $BA_{n>2}^-$ , proper calculations even with DFT approach became computationally too expensive. Therefore, we performed geometry optimization for  $BA_3^-$ , without any preliminary exploratory calculations, taking as a starting geometry the minimum energy structure of  $BA_2^-$  with an additional BA molecule placed on top in *nu* structural motif. The resulting optimal structure shown in Figure 4.6 is not much different from the starting geometry. The structure belongs to  $C_{2h}$  symmetry point group. In Figure 4.7(c) we show the contour plot of HOMO of  $BA_3^-$ , which reveals the same pattern we saw for  $BA_2^-$ . The MO has  $\pi$  bonding character along central C-C bond and  $\pi^*$  antibonding character along C-O bonds of each BA molecule. The  $\pi$  lobes along central C-C bonds in each BA molecule overlap creating an electron den-

sity between BA molecules. However, this time the excess electron is delocalized over three BA molecules, creating two order-of-1/4 bonds that hold the cluster together. This is consistent with the fact that the distance (3.07 Å) between adjacent BA molecules, defined as the distance between middle points of central C-C bonds, is longer than the distance (2.89 Å) between BA molecules in BA<sub>2</sub><sup>-</sup>.

#### 4.4.2 Energies

For BA<sub>2</sub><sup>-</sup> and BA<sub>3</sub><sup>-</sup>, we calculated VDEs and solvation energies  $E_{\text{solv}}$  at the M06-2X/aug-cc-pVDZ level of theory. We show the results in Table 4.3, along with some derived quantities and relevant experimental results. VDEs were calculated, just like for BA<sup>-</sup>, as a difference between the ground state energy of the anion and the energy of the corresponding neutral species at the equilibrium geometry of the anion. Solvation energies  $E_{\text{solv}}(n)$  were calculated using the formula

$$E_{\text{solv}}(n) = E(\text{BA}^-) + (n - 1)E(\text{BA}) - E(\text{BA}_n^-).$$

In other words, solvation energy is the energy required to assemble the cluster anion BA<sub>n</sub><sup>-</sup> out of BA<sup>-</sup> and a sufficient number of neutral BA molecules. The usage of the term "solvation" here is purely formal, and not intended to describe the nature of the intermolecular interactions in cluster anions.

VDEs given by M06-2X overestimate experimental VDEs, corresponding to band peaks, by about 0.2-0.3 eV. However, the differences between VDEs match the band shifts much better. Espe-

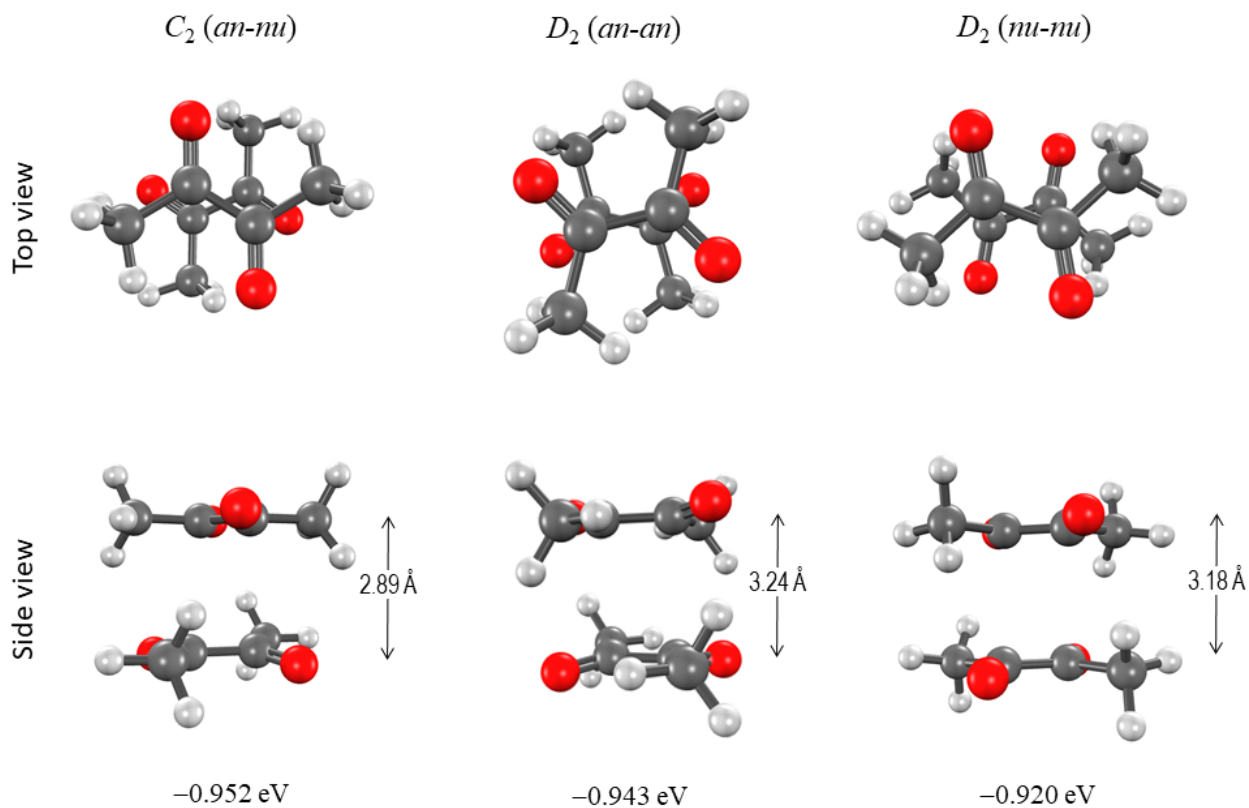


Figure 4.5:  $(\text{BA})_2^-$  structures optimized at the M06-2X level of theory with the aug-cc-pVDZ basis set. The  $C_2$  (*an-nu*) structure consists of one BA moiety adopting the “anion” (*an*) structural motif and one BA moiety adopting the “neutral” (*nu*) motif (the motifs are defined in Figure 4.4). In the  $C_2$  (*an-nu*) structure shown, the *an*-moiety is in the front of the top view and at the top of the side view. The total Mulliken charges of the *an* and *nu* BA moieties in this structure are  $-0.52$  and  $-0.48$ , respectively. The  $D_2$  (*an-an*) and  $D_2$  (*nu-nu*) structures consist of two equivalent *an*-BA and two equivalent *nu*-BA moieties, respectively, each moiety in each case carrying a Mulliken charge of  $-0.5$ . The separations between the monomer groups indicated in the figure (side views) are defined as the distance between the centers of the respective C2-C3 bonds (see Figure 4.4 for atom numbers). Complete dimer anion structures are included in the Supporting Information. The energy of each structure shown is the negative of the cluster solvation energy, defined relative to the adiabatic  $\text{BA} + \text{BA}^-$  dissociation limit (see footnote *a* in Table 4.3).

Table 4.2: Vertical and adiabatic energies (in eV) of the singlet ( $X^1A_g$ ) and triplet ( $a^3A_u$ ) electronic states of biacetyl relative to the  $BA^-$  anion ( $X^2A_u$ ) equilibrium.

method <sup>a</sup>	singlet ( $X^1A_g$ )		triplet ( $a^3A_u$ )	
	vertical (VDE)	adiabatic (EA)	vertical (VDE)	adiabatic (EA)
M06-2X <sup>b</sup>	1.379	0.802	3.410	3.268
CCSD <sup>b</sup>	1.092	0.545	3.369	3.248
EOM-IP-CCSD <sup>c</sup>	1.037		3.114	
experiment	1.12(5)	<0.7	3.17(2)	3.05(5)

<sup>a</sup>All calculations used the aug-cc-pVDZ basis set. <sup>b</sup>The relative state energies were obtained by subtracting the anion energy from the corresponding (vertical or adiabatic, as appropriate) neutral state energy. <sup>c</sup>The single-point EOM-IP calculations employed the doublet ( $^2A_u$ ) anion reference and were carried out for the CCSD/aug-cc-pVDZ optimized geometry of the anion. The vertical singlet-state excitation energy was calculated by considering the lowest-energy alpha-spin electron-removal transition of  $A_u$  symmetry ( $^2A_u \rightarrow ^1A_g$ ), while the triplet-state energy was calculated using the corresponding beta-spin transition of  $A_g$  symmetry ( $^2A_u \rightarrow ^3A_u$ ).

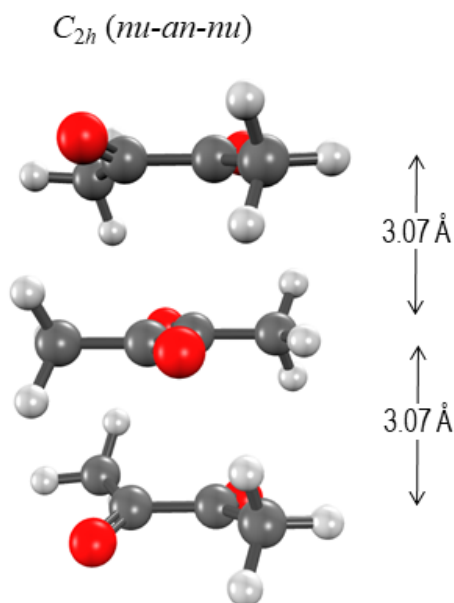


Figure 4.6: A plausible  $(BA)_3^-$  structure optimized at the M06-2X level of theory with the aug-cc-pVDZ basis set. The structure is of  $C_{2h}$  symmetry and adopts a nu-an-nu structural motif. The complete structure with all coordinates is included in the Supporting Information. The distribution of the Mulliken charges between the top-middle-bottom BA moieties in this structure is  $-0.285$ ,  $-0.43$ ,  $-0.285$ . The distance between the middle and top/bottom monomer moieties, defined the same way as in Figure 4.5, is  $3.07 \text{ \AA}$ . The energy of this structure (defined as the negative of the solvation energy) is  $-1.670 \text{ eV}$ , i.e., it is  $1.670 \text{ eV}$  more stable than the  $2BA + BA^-$  dissociation limit (see Table 4.3).

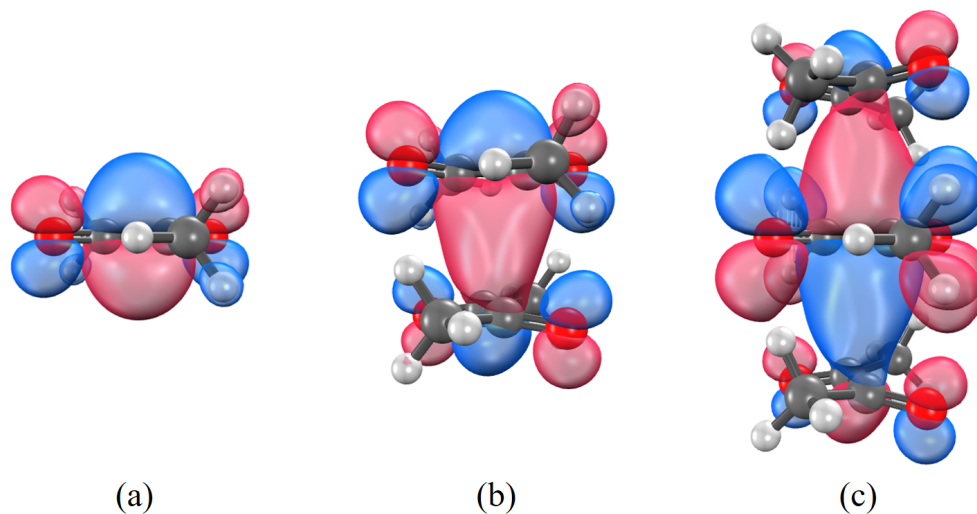


Figure 4.7: Highest occupied molecular orbitals of (a)  $\text{BA}^-$  (the *an* structure shown in Figure 4.4, bottom), (b)  $(\text{BA})_2^-$  (the *an-nu* structure shown in Figure 4.5, left), and (c)  $(\text{BA})_3^-$  (the *nu-an-nu* structure shown in Figure 4.6). Different perspectives (viewpoints) have been chosen in this figure, compared to the above figures. The orbital plots are from the M06-2X/aug-cc-pVDZ calculations and correspond to the isosurface values of (a) 0.10, (b) 0.08, and (c) 0.05. The MOs shown are singly occupied in the respective anions and responsible for the  $\pi - \pi$  covalent bonding between the individual BA moieties in the dimer and trimer anions.

cially, the difference 0.569 eV between  $VDE(BA^-)$  and  $VDE(BA_2^-)$  perfectly matches the corresponding band shift 0.59(1) eV. This outcome is not unexpected, considering that M06-2X functional is specifically designed to treat intermolecular interactions well. On the other hand,  $VDE(BA^-)$  is perfectly predicted by ab initio CCSD method, as discussed in Subsection 4.3.2. This motivates CCSD+DFT approach that uses ab initio CCSD method to account for intramolecular interactions and DFT approach with M06-2X functional for intermolecular ones. Specifically, in CCSD+DFT approach we calculate VDEs of  $BA_{n=2,3}^-$  by adding the  $VDE = 1.092$  of BA determined using the CCSD method to the corresponding band shifts (relative to  $BA^-$ ) determined using the M06-2X method. By construction, the predictions of this approach perfectly match the experimental results (See Table 4.3).

The sequential  $\Delta VDE$  from  $BA_2^-$  to  $BA_3^-$  is larger than the corresponding sequential band shift by about 0.1 eV. This discrepancy is almost an order of magnitude larger than the error, which is about 0.02 eV, for the shift from  $BA^-$  to  $BA_2^-$ . We can only speculate that it indicates that the true trimer structure is probably a combination of the distributed-charge character predicted by DFT and a somewhat weaker bonded ion-molecule complex.

For typical cluster anions, the effect of intermolecular interactions on the electronic structure of constituents is negligible and the interaction between the neutral constituents in the final state is weak. As a result, the experimental band shifts often correspond to solvation energies. However, this is not the case for the cluster anion of BA. The calculated solvation energies greatly overestimate the experimental band shifts, the discrepancy being about 0.4-0.5 eV. It should be noted that such a large discrepancy cannot be attributed to computational inaccu-

racy, since  $\Delta$ VDEs obtained using the same methodology matched the experimental band shifts quite well.

In Figure 4.8, we illustrate, in the example of  $\text{BA}_2^-$  how the different quantities considered here are interrelated. The conclusion is true regardless of the computational method used and can be easily generalized to larger cluster anions of BA. In particular, the diagram shows why the solvation energies are considerably larger than  $\Delta$ VDE values.

## 4.5 Conclusions

We presented our experimental study of BA anion and its cluster anions conducted using photoelectron imaging spectroscopy and supported by calculations. The results of ab initio computational investigation of electronic structure of BA and its anion were very successful in explaining the features of BA spectra. The calculations showed that the HOMO of BA anion has  $\pi$  bonding character along the central C-C bond and  $\pi^*$  antibonding character along the C-O bonds. DFT calculations showed that the high electron density along the central C-C bond of BA enables formation of its smaller cluster anions. Specifically, in  $\text{BA}_2^-$  and  $\text{BA}_3^-$ , the monomers are held together by  $\pi - \pi$  intermolecular interactions. These interactions have strong covalent character, which explains large band shifts observed for the cluster anions.

Table 4.3: Vertical detachment energies, band shifts, and cluster solvation energies (all in eV), calculated using the M06-2X/aug-cc-pVDZ Method for the  $(\text{BA})_n^-$  cluster anions.

	$\text{BA}^-$	$(\text{BA})_2^-$	$(\text{BA})_3^-$	$(\text{BA})_4^-$
Solvation energy (DFT) <sup>a</sup>	0	0.952	1.670	– <sup>b</sup>
VDE				
DFT <sup>c</sup>	1.379 <sup>d</sup>	1.947	2.512	–
(CCSD+DFT) <sup>e</sup>	1.092	1.661	2.226	–
Experiment <sup>f</sup>	1.12(5)	1.71(5)	2.16(5)	2.46(5)
$\Delta\text{VDE}$ (DFT)				
Relative to $\text{BA}^-$ <sup>g</sup>	n/a	0.569	1.134	–
Sequential <sup>h</sup>	n/a	0.569	0.565	–
Band shift (experiment) <sup>i</sup>				
Relative to $\text{BA}^-$ <sup>g</sup>	n/a	0.59(1)	1.04(1)	1.34(1)
Sequential <sup>h</sup>	n/a	0.59(1)	0.45(1)	0.30(1)

<sup>a</sup>Solvation energies for the  $(\text{BA})_n^-$  cluster anions (up to  $n = 3$  only) were calculated as  $E_{\text{solv}}(n) = E[\text{BA}^-] + (n - 1)E[\text{BA}] - E[(\text{BA})_n^-]$ . The energies of all species were calculated for the corresponding optimized ground-state structures: the  $C_{2h}$  (an) and  $C_{2h}$  (nu) geometries of  $\text{BA}^-$  and  $\text{BA}$ , respectively (as defined in Figure 4.4), and the  $C_2$  (an-nu) geometry of the dimer anion (shown in Figure 4.5).

<sup>b</sup>Dashes indicate that the corresponding property was not calculated for the given species; n/a indicates that the property is not applicable to this species.

<sup>c</sup>The vertical detachment energy (VDE) for each ion is calculated as the difference between the neutral and anion energies, both determined at the optimized geometry of the anion.

<sup>d</sup>For comparison, the VDE values for  $\text{BA}^-$  calculated at the CCSD and EOM-IP-CCSD levels of theory are 1.092 and 1.037 eV, as summarized in Table 4.2. These results are in much better agreement with the experiment, compared to the DFT value.

<sup>e</sup>The VDE (CCSD + DFT) values were determined by adding the VDE = 1.092 eV of  $\text{BA}^-$  determined using the CCSD method to the corresponding  $(\text{BA})_n^-$  band shifts (relative to  $\text{BA}^-$ ), determined using the M06-2X DFT method, also included in this table.

<sup>f</sup>From the data in Figure 3(a).

<sup>g</sup>  $\Delta\text{VDE}$  (DFT) for a particular  $(\text{BA})_n^-$  cluster is determined as the difference between this cluster's VDE and that of  $\text{BA}^-$ :  $\Delta\text{VDE}(n) = \text{VDE}(n) - \text{VDE}(1)$ .

<sup>h</sup>Same as above but relative to the preceding member of the series:  $\Delta\text{VDE}(n) = \text{VDE}(n) - \text{VDE}(n - 1)$ .

<sup>i</sup>From the fits in Figure 4.3.

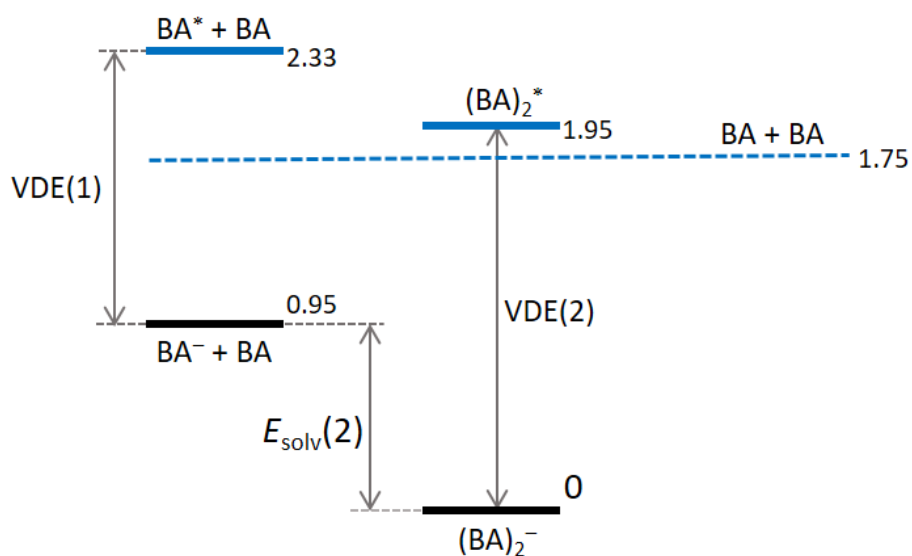


Figure 4.8: Energy diagram for the formation and photodetachment of the  $(\text{BA})_2^-$  cluster anion. The electronic energy values calculated using the M06-2X/aug-cc-pVDZ method are given in eV relative to  $(\text{BA})_2^-$ . The diagram shows that the VDE increase from  $n = 1$  to  $n = 2$  in the  $(\text{BA})_n^-$  series,  $\Delta\text{VDE}(2) = \text{VDE}(2) - \text{VDE}(1)$ , cannot be used as an accurate estimate of  $E_{\text{solv}}(2)$ .

# Chapter 5

## Oxalyl chloride

Oxalyl chloride,  $(\text{COCl})_2$ , is a versatile organic reagent, widely used in chlorination, oxidation, reduction, dehydration, decarboxylation, and formylation reactions [49]. It is related and often compared to phosgene,  $\text{COCl}_2$ , but this chapter pursues an alternative perspective viewing oxalyl chloride as a member of the substituted-glyoxal family (Figure 1.1).

Despite the structural and photochemical properties of oxalyl chloride that pique a physical chemist's interest, the spectroscopic literature on this molecule and especially its anion is sparse. This is due, in part, to the dangerous properties of this compound. Fortunately, there are previous spectroscopic studies of it. In the experiment by Chu et al. [50], parent and fragment cation yields for oxalyl chloride were measured using synchrotron radiation, allowing the authors to estimate that anti and gauche were the two conformers present in the gas phase ( $\sim 70\%$  and  $\sim 30\%$ , respectively), with no contribution from the syn conformer. A valence-shell photoelec-

tron spectrum of neutral oxalyl chloride in the photon-energy range of 19-91 eV was reported recently by Holland et al. [51] There have been several determinations of the ionization energy, 10.91(5) eV adiabatic value [52, 53]. Below the ionization threshold, the UV/vis absorption spectrum of oxalyl chloride shows an onset at about 390 nm [54–56]. In 1997, Suits and coworkers exploited one feature of the absorption spectrum to study the gas-phase photochemistry of oxalyl chloride near 235 nm. Using photofragment ion imaging, they discovered that the  $(\text{COCl})_2$  molecule dissociates into four fragments following the absorption of just one UV photon [57].

In the present chapter, we focus on the anion of oxalyl chloride. There is currently a dearth of information about its most fundamental properties. Using photoelectron imaging spectroscopy and ab initio calculations, we illuminate some of the anion's features, including its photoelectron spectrum and detachment energy, as well as the electron affinity (EA) of neutral oxalyl chloride. The spectroscopic results for this anion are compared to the results for glyoxal [16], methylglyoxal [17], and biacetyl [15].

## 5.1 Geometric structures

Since little prior information is available about the anion of oxalyl chloride, we begin with the analysis of its geometric structures. After these basic properties are defined, we will turn to the spectroscopic investigation using anion photoelectron imaging, as described in the next section.

The Lewis structure of the neutral  $(\text{COCl})_2$  molecule (Figure 1.1) allows for a nearly free internal

rotation about the C-C sigma bond with respect to the Cl-C-C-Cl dihedral angle,  $d$ . The torsional potential is rather flat but does have a few defined minima [50]. The structure in Figure 1.1 ( $C_{2h}$  symmetry,  $d = 180^\circ$ ) corresponds to the most stable *anti* conformer. We clearly delineate the *anti* vs *trans* and *syn* vs *cis* structures. Although these terms are sometimes used interchangeably, this practice would lead to a lack of clarity in the present investigation. In short, the *anti*, *gauche*, and *syn* structures correspond to neutral oxalyl chloride, while *trans* and *cis* to the anion. The *anti* conformer in Figure 1.1 should not be referred to as a *trans* isomer because its geometry is not "locked" with respect to internal rotation. Similarly, the alternative plane structure ( $C_{2v}$  symmetry,  $d = 0^\circ$ ) corresponds to the *syn* conformer, not *cis* isomer. An intermediate structure of  $C_2$  symmetry ( $0^\circ < d < 180^\circ$ ) corresponds to a *gauche* conformation.

Previous studies in the gas phase revealed the coexistence of the *anti* and *gauche* conformers of oxalyl chloride, with no contribution from *syn* [50, 58]. For the *gauche* conformer, electron diffraction experiments indicated  $d = 55(6)$  or  $76(18)^\circ$ , depending on the study [58, 59], while the *ab initio* values range between  $d = 87$  or  $91^\circ$ , depending on the method [60, 61]. It is important for the present work that the majority of neutral oxalyl chloride is found in the *anti* form, but the *gauche* conformer, which is only 0.04 eV less stable, still accounts for a significant mole fraction ( $\sim 30\%$  at  $0^\circ\text{C}$ ) [58, 59]. The *syn* structure, another 0.05 eV higher than *gauche* [50], is not a true potential minimum but a saddle point separating the equivalent *gauche* conformers at  $d \approx \pm 90^\circ$ .

The anion of oxalyl chloride differs significantly from the neutral because of the additional half-bond of  $\pi$  character between the carbon atoms. The highest- (singly-) occupied molecular or-

bital (HOMO) of the  $C_{2h}$  symmetry anion structure (details to follow) is shown in Figure 5.1. Its  $\pi$ -bonding character with respect to the C-C bond shortens this bond in the anion and locks the structure with respect to internal rotation, resulting in potential minima at  $d = 180^\circ$  ( $C_{2h}$ ) and  $0^\circ$  ( $C_{2v}$ ). It also precludes the existence of intermediate ( $0^\circ < d < 180^\circ$ ) minimum on the anion potential. Although the  $C_{2h}$  and  $C_{2v}$  anion structures look similar to the respective *anti* and *syn* conformations of neutral oxalyl chloride, they cannot easily interconvert and should therefore be referred to as the *trans* and *cis* isomers, rather than *anti* and *syn* conformers.

These preliminary considerations are confirmed by the electronic structure calculations using the Q-CHEM 5.1 program package [46]. Some of the key results are summarized in Figure 5.2. The initial geometry optimizations and potential energy scans were performed using the B3LYP density functional with the aug-cc-pVDZ basis set. As expected, a cursory scan of the anion potential with respect to  $d$  (relaxed with respect to other coordinates under the  $C_2$  symmetry constraint) indicated a  $>1$  eV barrier separating the *trans* and *cis* forms of  $(\text{COCl})_2^-$ . The barrier, indicated schematically by the dashed gray curve in Figure 5.2, is large enough for us to not be concerned about its exact magnitude. For this reason, higher-level investigations of the *trans*  $\leftrightarrow$  *cis* interconversion were not pursued.

The *trans*- and *cis*-anion geometries, as well as the global-minimum neutral structure (*anti*), were optimized using the coupled-cluster theory with single and double excitations (CCSD). Initial CCSD optimizations employed the aug-cc-pVDZ basis set, followed by further optimizations with the aug-cc-pVTZ basis. The final state energies were determined from the single-point calculations including the noniterative triples corrections, CCSD(T), with the aug-cc-

pVTZ basis set. The complete geometric parameters of CCSD/aug-cc-pVTZ-optimized *trans* ( $C_{2h}$ ) and *cis* ( $C_{2v}$ ) anion structures are given in Table 5.1. In Figure 5.2 and throughout, we refer to these geometries as simply *trans* and *cis*, thus distinguishing them from the respective *anti* and *syn* neutral structures. The optimized parameters of the neutral *anti* conformer are also included in Table 5.1.

## 5.2 Experimental results

The mass spectrum of  $(\text{COCl})_2^-$  anions consists of a triplet of peaks at 126, 128, and 130 amu with a characteristic  $\sim 9 : 6 : 1$  intensity ratio due to the approximately 3:1 abundance ratio of the  $\text{Cl}^{35}$  and  $\text{Cl}^{37}$  isotopes. A sample parent-ion spectrum is shown in Figure 5.3. The most intense 126 amu peak was used in the photoelectron imaging experiments.

Before describing the spectroscopic results, it is important to consider the implications of the large torsional barrier on the anion potential in oxalyl chloride (Figure 5.2). Based on the previous studies [50, 58], we must assume the presence of both *anti* and *gauche* conformers of neutral  $(\text{COCl})_2$  in the precursor expansion. It is not clear what temperature should be ascribed to the neutral molecules just before the anion formation. Since it occurs within the electron-impact ionized plasma, the process cannot be modeled using the typical supersonic temperature of a few Kelvin. It is reasonable to expect that the *anti* conformer yields predominantly *trans*- $(\text{COCl})_2^-$ , while *gauche* can generate either *trans*- and *cis*-anions, likely in similar quantities. If we assume a 0.70/0.30 *anti/gauche* ratio for the neutral precursor [58, 59],  $\sim 0.85$  and

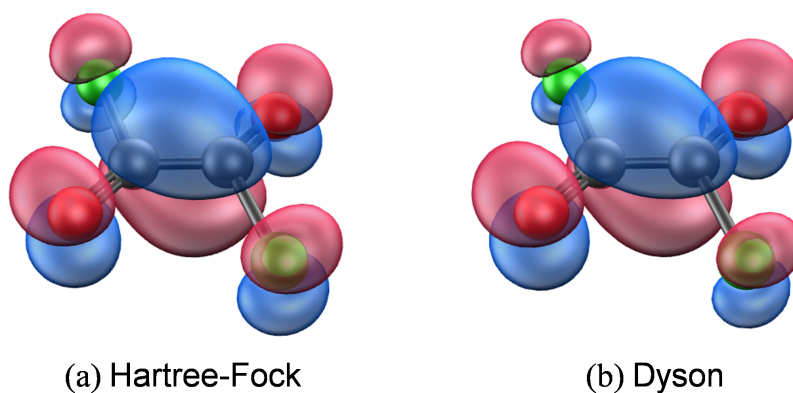


Figure 5.1: (a) Hartree-Fock (HF)  $4a_u$  HOMO of the oxalyl chloride anion (trans structure). (b) The Dyson orbital for the  $X^2A_u \rightarrow X^1A_g$  photodetachment transition, nominally  $(4a_u)^{-1}$ , calculated using the EOM-IP-CCSD method. Both orbitals are represented by the 0.04 au isosurface plots and were calculated using the aug-cc-pVTZ basis set.

Table 5.1: Geometric parameters of the *anti* ( $C_{2h}$  symmetry), *trans* ( $C_{2h}$ ), and *cis* ( $C_{2v}$ ) structures<sup>a</sup> of oxalyl chloride

	<i>anti</i>	<i>trans</i>	<i>cis</i>
C-C	1.549	1.423	1.430
C-O	1.182	1.219	1.221
C-Cl	1.746	1.844	1.837
$\angle$ C-C-Cl	112.2°	110.2°	117.2°
$\angle$ C-C-O	123.9°	131.8°	125.8°

<sup>a</sup>The *trans* and *cis* structures correspond to anion equilibria, while the *anti* is the global-minimum geometry of the neutral molecule. All structures were optimized at the CCSD level of theory with the aug-cc-pVTZ basis set. The bond lengths are given in Angstroms, and bond angles are given in degrees.

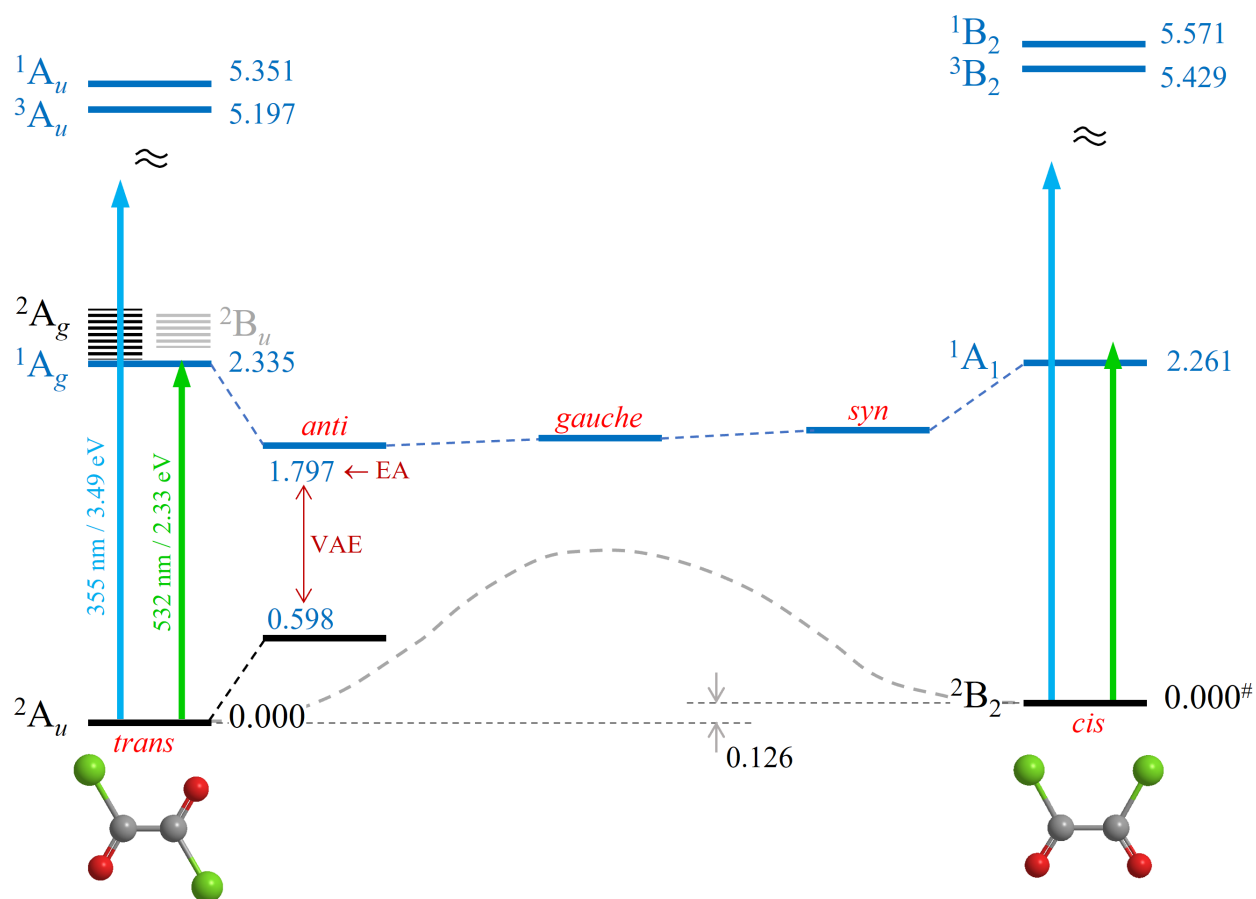


Figure 5.2: Energy diagram summarizing the results of the calculations. All energy values are in electron-volts. The values on the left (*trans/anti*) side are relative to the *trans*-anion structure. The values on the right (*cis*) are reported relative to the *cis*-anion (#). See the text for details. All neutral state energies at the *trans*- and *cis*-anion geometries correspond to the vertical detachment energy (VDEs). The *anti*-neutral state energy, relative to the *trans*-anion equilibrium, is the adiabatic EA. The difference between the neutral and anion energies at the *anti*-neutral geometry (indicated by the double-sided arrow) is the vertical attachment energy (VAE).

$\sim 0.15$  mole fractions of the *trans*- and *cis*-anions should be expected. Once the anions are cooled to a typical ion-beam temperature of  $\sim 70\text{K}$  [21], the torsional barrier makes the *cis*  $\leftrightarrow$  *trans* interconversion unlikely. In sum, while it is difficult to predict the exact populations, the *trans* isomer is expected to dominate, but some fraction of the anions may be trapped in the *cis* state.

Figure 5.4 shows the photoelectron images and spectra obtained at 355 and 532 nm. Figure 5.4a displays both spectra plotted together for comparison. Figure 5.4b,c separates the spectra and compares them to the model simulations. Figure 5.4b,c also includes the original photoelectron images from which the spectra were obtained. The right and left halves of the image in Figure 5.4b corresponds to the raw and Abel-inverted data, respectively.

The 355 nm spectrum (Figure 5.4a,b) consists of a single broad band assigned to the electronic transition from the ground state of the anion to the ground state of neutral oxalyl chloride. The width of the band indicates a significant difference between the equilibrium geometries of these states. The band maximum at about 2.3 eV corresponds to the anion's vertical detachment energy (VDE). The poorly defined onset at approximately 1.8 eV corresponds to the adiabatic electron affinity (EA) of oxalyl chloride. The 532 nm spectrum (Figure 5.4a,c) at first glance looks like the lower-energy part of the 355 nm band if it were split almost evenly into two halves. However, the sharp onset of the 532 nm spectrum at  $e\text{BE} \rightarrow h\nu$ , corresponding to low-eKE electrons, is uncharacteristic of regular photodetachment and requires further analysis (Subsection 5.3.2).

The photoelectron angular distributions (PADs) [62–64] with respect to the laser polarization direction were obtained from the photoelectron images using the BASEX program [26]. For the 355 nm data, the PAD was determined by integrating the angle-dependent image intensity over the nearly complete energy range of the band (Figure 5.4a,b),  $eBE = 1.70\text{-}2.79$  eV. The angular dependence of the 532 nm data was analyzed in the range of  $eBE = 1.86\text{-}2.16$  eV. The lower bound corresponds to  $eBE$  where the band intensity increases more than 2-fold above the noise level. The upper bound was chosen specifically to exclude the slow-electron signal at the image center, corresponding to the sharp peak at  $eBE \rightarrow h\nu$ . In Subsection 5.3.2, this threshold spike will be attributed to a different photodetachment mechanism, compared to the rest of the 532 nm image.

The photoelectron anisotropy parameter ( $\beta$ ) values determined as described above are plotted in Figure 5.5 against the corresponding average  $eKEs$ . The large horizontal "error bars" for the two data points are neither errors nor uncertainties: they indicate the respective energy intervals over which the PADs were analyzed (see above). The vertical error bars in each case do indeed represent the statistical uncertainties in determining the  $\beta$  values from the experimental data.

## 5.3 Electronic structure

### 5.3.1 Bound States

The oxalyl chloride anion is obtained by adding an electron to the closed-shell neutral molecule. According to the calculations in Section 5.1, *trans*-(COCl)<sub>2</sub> has an  $X^2A_u$  ground state with the electron configuration  $[X^1A_g](4a_u)^1$ , where  $X^1A_g$  is the neutral state. The  $4a_u$  orbital is shown in Figure 5.1a, and all relevant electron configurations are expanded in Tables 5.2 and 5.3. The ground state of the *cis*-anion is  $X^2B_2 : [X^1A_1](4b_2)^1$  (Table 5.3). The  $B_2$  irreducible representation is defined assuming that the molecular plane is the primary  $\sigma_v$  mirror plane.

Using the CCSD(T) results in Section 5.1, the adiabatic EA, the relative energies of the anion isomers, and the vertical attachment and detachment energies can be calculated from the differences,  $\Delta\text{CCSD(T)}$ , of the appropriate state energies. These results are included in Tables 5.2 and 5.3. Table 5.2 lists the anion and neutral state energies, each calculated for the  $C_{2h}$  *trans* and *anti* geometries (Table 5.1). As discussed in Section 5.1, these are the equilibrium geometries of the anion and neutral, respectively. Therefore, the energy difference between the *anti*-neutral and *trans*-anion structures corresponds to adiabatic EA of the neutral. The differences between the *trans*-neutral states and the *trans*-anion are the VDEs of the anion for transitions to these neutral states. Finally, the differences between the *anti*-neutral and *anti*-anion is the vertical attachment energy (VAE) of the neutral. Table 5.3 lists the relative state energies at the *cis* geometry only, i.e., all values in the table represent the VDEs for the *cis*-anion transitions to

different neutral states.

Thus determined EA = 1.797 eV (Table 5.2) for *anti*-oxalyl chloride agrees with the observed onsets of the detachment bands in Figure 5.4. The VDE of the *trans*-anion, calculated using the  $\Delta$ CCSD(T) method, is 2.284 eV, matching closely the position of the maxima of the 355 nm and 532 nm bands in Figure 5.4. The  $\Delta$ CCSD(T) results further predict that the ground state of the *cis*-anion is 0.126 eV higher in energy than the *trans* minimum (Figure 5.2) and has a VDE of 2.219 eV.

The  $\Delta$ CCSD(T) results are in good agreement with the experiment, but they do suffer from the shortcoming of relying on different electronic wave function references to describe the anion and neutral states [47]. The problem is resolved within the equation-of-motion (EOM) approach. To model the photodetachment transitions, we performed single-point EOM-XX-CCSD/aug-cc-pVTZ ionization-potential (XX = IP) and electron affinity (XX = EA) calculations [47] for the *trans* and *cis* geometries. In the IP calculations, an  $\alpha$ - or  $\beta$ -spin electron, as appropriate, was removed from the unrestricted  $X^2A_u/X^2B_2$  (*trans/cis*) anion reference, giving access to the ground and lowest-excited states of neutral oxalyl chloride. The EA transitions were analyzed by adding an  $A_u/B_2$  symmetry electron to the closed-shell (restricted)  $X^1A_g/X^1A_1$  neutral reference, yielding the  $X^2A_u/X^2B_2$  states of the anion. The noniterative triples corrections (fT) [65] were included in the IP transition energies for the *trans*-anion. Technical issues prevented us from directly calculating the fT corrections for the *cis* structure, so the *trans* fT values for the corresponding neutral states were used instead. The results (corresponding to the anion VDEs) are summarized in Tables 5.2 and 5.3 structures, respectively. Among the different methods, the

recommended values are bolded. These quantities were used to construct the energy diagram in Figure 5.2.

For the lowest-energy photodetachment transition in the dominant *trans* form of the anion, all results in Table 5.2 are in agreement with the experimental spectra in Figure 5.4. The highest-level, EOM-IP-CCSD(fT), energy for the  $X^2A_u \rightarrow X^1A_g$  transition, 2.335 eV, slightly overestimates the VDE determined from the experiment. These calculations also predict the lowest triplet ( $^3A_u$ ) and the corresponding open-shell singlet ( $^1A_u$ ) states of the neutral to lie 5.197 and 5.351 eV (vertically) above the *trans*-anion ground state. These transition energies are not accessible with our laser, but taken together with the ground-state VDE, they translate into a 2.862 eV singlet-triplet ( $S_0 \rightarrow T_1$ ) and a 3.016 eV singlet-singlet ( $S_0 \rightarrow S_1$ ) vertical excitation energies for the *trans*-anion of oxalyl chloride. These results can be indirectly but favorably compared to the corresponding adiabatic values for the *anti*-oxalyl chloride determined from the UV/vis absorption: 3.022 eV ( $S_0 \rightarrow T_1$ ) and 3.371 eV ( $S_0 \rightarrow S_1$ ) [66].

### 5.3.2 Anionic Resonances

The intense signal at the  $eBE \rightarrow h\nu$  ( $eKE \rightarrow 0$ ) threshold in 532 nm spectrum (Figure 5.4) may be a signature of autodetachment from an excited anionic state (a resonance) embedded in the detachment continuum [67, 68]. To investigate this possibility, we carried out several types of EOM-CCSD studies [47] targeting electronically excited states of the oxalyl chloride anion at its dominant *trans* geometry. First, the excitation energy (EE) methodology, EOM-EE-CCSD/aug-

cc-pVTZ, was used to identify the excited states of the anion by means of one-electron spin-conserving excitations from the  $X^2A_u$  anion reference. Second, the EOM-EA-CCSD calculations, where we add an electron to the  $X^1A_g$  neutral reference, were extended to target not only the ground state of the anion (Table 5.2) but also the excited states. Third, these states were characterized within the non-Hermitian quantum-mechanical framework using a complex absorbing potential (CAP) with the EOM-EA-CCSD method [69–72]. The last approach was necessary, because all electronically excited states of the *trans*-anion proved to be unbound resonances, i.e. they lie above the anion's vertical detachment threshold. Similar calculations for the *cis*-anion led to the same conclusion.

The details of these calculations for the *trans*-anion structure are summarized in the Supporting Information for reference [18]. The main conclusion is that there are indeed low-lying anionic states embedded in the detachment continuum close to the anion VDE and, by coincidence, the 532 nm photon energy. The two lowest excitation transitions give rise to the  $^2B_u$  and  $^2A_g$  resonances, which are indicated schematically in Figure 5.2. The  $^2B_u$  state is optically "dark", i.e., not accessible from the  $X^2A_u$  state of the anion via a one-photon electric-dipole transition, while  $^2A_g$  is dipole-allowed and, therefore, "bright". Their energies, calculated using different methods and basis sets, are listed in the Supporting Information for reference [18].

Specifically, the CAP-EOM calculations place the  $^2A_g$  resonance  $\sim 0.3$  eV above the neutral and  $\sim 2.4$  eV above the anion ground state. On comparing the latter to the 2.33 eV energy of 532 nm photons, the resonance width ( $\sim 0.3$  eV) and the unknown Franck-Condon width of the  $X^2A_u \rightarrow ^2A_g$  transition should be kept in mind. Therefore, the  $^2A_g$  resonance is likely to be accessible

from the *trans*-anion ground state with 532 nm photons. It may be also be vibronically coupled to the dark  ${}^2B_u$  state or to the dense highly vibrationally excited levels of the  $X^2A_u$  state, setting up plausible pathways for vibrationally mediated autodetachment.

## 5.4 Photoelectron angular distributions

The PADs give insight into the electronic structures, in particular, the orbitals from which the emitted electrons originate [62–64, 73–76]. The dominant transition in this work nominally corresponds to electron removal from the  $4a_u$  HOMO of the *trans*-anion of oxalyl chloride. This Hartree-Fock orbital is depicted in Figure 5.1a. While it is a good start for describing the PADs, the HOMO is not the only MO participating in the transition. The removal of the canonical HOMO electron affects all electrons in the molecule (as a basis example, the 1s orbital in the H atom is not the same as 1s in  $H^-$ ). Although the detachment of a single electron is not a one-electron process, it is possible to describe it as such using the corresponding Dyson orbital instead of the canonical MO. The Dyson orbital is defined as the overlap between the anion and neutral many-electron wave functions; it thus encodes the changes to all MOs upon the anion  $\rightarrow$  neutral transition [76]. The Dyson orbital for  $X^2A_u \rightarrow X^1A_g$  photodetachment of oxalyl chloride, obtained as part of the EOM-IP-CCSD calculations, is shown in Figure 5.1b. By inspection, only minor differences between the canonical and Dyson orbitals can be seen. These differences, however, do affect the quantitative modeling of the PADs.

In Figure 5.5, we compare the experimental  $\beta$  values, determined in Section 5.2, to the pre-

Table 5.2: Nominal electron configurations and relative energies of the ground electronic state of oxalyl chloride anion and several lowest electronic states of neutral oxalyl chloride at  $C_{2h}$  *trans* and *anti* geometries

nominal electron configuration state character	geometry <sup>a</sup>	method <sup>b</sup>	rel. energy <sup>c</sup>
$X^2A_u : \dots (13a_g)^2 (3b_g)^2 (3a_u)^2 (12b_u)^2 (4a_u)^1$ anion ground state	<i>trans</i>		0
	<i>anti</i>	$\Delta$ CCSD	0.565
		$\Delta$ CCSD(T)	0.598
$X^1A_g : \dots (13a_g)^2 (3b_g)^2 (3a_u)^2 (12b_u)^2$ closed-shell singlet	<i>anti</i>	$\Delta$ CCSD	1.755
		$\Delta$ CCSD(T)	<b>1.797</b>
	<i>trans</i>	$\Delta$ CCSD	2.340
		$\Delta$ CCSD(T)	2.284
		EA-CCSD	2.267
		IP-CCSD	2.414
		IP-CCSD(fT)	<b>2.335</b>
		VDE (exper.)	2.33(4)
$a^3A_u : \dots (12a_g)^2 (3b_g)^2 (3a_u)^2 (12b_u)^2 (13a_g)^1 (4a_u)^1$ lowest triplet	<i>trans</i>	IP-CCSD	5.259
		IP-CCSD(fT)	<b>5.197</b>
		EA-CCSD	5.133
$A^1A_u : \dots (12a_g)^2 (3b_g)^2 (3a_u)^2 (12b_u)^2 (13a_g)^1 (4a_u)^1$ open-shell singlet	<i>trans</i>	IP-CCSD	5.433
		IP-CCSD(fT)	<b>5.351</b>

<sup>a</sup>The *trans* and *anti* structures correspond to the respective anion and neutral geometries optimized at the CCSD/aug-cc-pVDZ level. Their geometric details are summarized in Table 5.1. <sup>b</sup>All calculations in this table were carried out with the aug-cc-pVTZ basis set. The  $\Delta$ CCSD and  $\Delta$ CCSD(T) results were obtained as differences between the absolute CCSD or CCSD(T) energies of the target state and the *trans*-anion ground state, determined in separate calculations. Zero-point vibrational energy corrections are not included. Single-point EOM-XX-CCSD (XX = IP, EA) calculations, abbreviated as XX-CCSD, with or without fT corrections, were carried out for the *trans* geometry. The IP calculations were carried out by removing an  $\alpha$ - or  $\beta$ -spin electron, as appropriate, from the unrestricted  $X^2A_u$  anion reference. The EA transitions were analyzed by adding an electron to either the closed-shell (restricted)  $X^1A_g$  or the unrestricted  $a^3A_u$  neutral reference, as appropriate. The VDE (exper) value is determined from the model fits to the experimental photoelectron bands shown in Figure 5.4. <sup>c</sup>Energy values are given in electron-volts, relative to the *trans*-anion ground state. Recommended theory values in bold.

Table 5.3: Nominal electron configurations and relative energies of the ground electronic state of the oxalyl chloride anion and several lowest electronic states of the neutral at the *cis* geometry

nominal electron configuration	method <sup>a</sup>	rel. energy <sup>b</sup>
$X^2B_2 : \dots (13a_1)^2(3a_2)^2(12b_1)^2(3b_2)^2(4b_2)^1$ anion ground state	$\Delta$ CCSD	0
$X^1A_1 : \dots (13a_1)^2(3a_2)^2(12b_1)^2(3b_2)^2$ closed-shell singlet	$\Delta$ CCSD(T)	2.264
	EA-CCSD	2.197
	IP-CCSD	2.340
	IP-CCSD(fT)	<b>2.261</b>
$a^3B_2 : \dots (12a_1)^2(3a_2)^2(12b_1)^2(3b_2)^2(13a_1)^\uparrow(4b_2)^\uparrow$ lowest triplet	IP-CCSD	5.491
	IP-CCSD(fT)	<b>5.429</b>
$A^1B_2 : \dots (12a_1)^2(3a_2)^2(12b_1)^2(3b_2)^2(13a_1)^\uparrow(4b_2)^\uparrow$ open-shell singlet	IP-CCSD	5.663
	IP-CCSD(fT)	<b>5.571</b>

<sup>a</sup>All calculations were carried out with the aug-cc-pVTZ basis set. The  $\Delta$ CCSD and  $\Delta$ CCSD(T) results were obtained as differences between the absolute CCSD or CCSD(T) energies of the target state and the *cis*-anion ground state, determined in separate calculations. Zero-point vibrational energy corrections are not included. Single-point EOM-XX-CCSD (XX = IP, EA) calculations, abbreviated as XX-CCSD, with or without fT corrections, were carried out for the *cis*-anion geometry (Table 5.1). The IP calculations were carried out by removing an  $\alpha$ - or  $\beta$ -spin electron, as appropriate, from the unrestricted  $X^2B_2$  anion reference. The EA transitions were analyzed by adding an electron to the closed-shell (restricted)  $X^1A_1$  neutral reference. The fT corrections from the *trans* calculations (Table 5.2) are used here. <sup>b</sup>Energy values are in electron-volts, relative to the *cis*-anion ground state. Recommended values are in bold.

dictions of the ezDyson program by Gozem and Krylov [77, 78]. Both the HF and Dyson orbitals shown in Figure 5.1 were imported into ezDyson, and the eKE-dependent photoelectron anisotropy values were calculated for each MO by expanding the continuum state of the electron in partial waves up to  $l = 6$ . Figure 5.5 shows the resulting  $\beta(\epsilon)$  curves. The overall agreement between the model and the experiment is quite good. The slightly better apparent agreement of the HF curve with 355 nm data point should not be overinterpreted: the Dyson orbital is a rigorously more accurate approach to modeling the PADs [76].

## 5.5 Comparison to other anions in the glyoxal family

Figure 5.6 compares the published anion photoelectron spectra of biacetyl (532 nm) [15], methylglyoxal (612 nm) [17], and glyoxal (532 nm) [16] to the results for oxalyl chloride (355 nm). Each spectrum consists of a single band due to the photodetachment from the ground state of the anion to the ground state of the neutral.

The electron affinities and detachment energies follow the trend: biacetyl < methylglyoxal < glyoxal << oxalyl chloride. Specifically, the anion VDEs are 1.12(5) eV for biacetyl, 1.20(4) eV for methylglyoxal, 1.30(4) eV for glyoxal, and 2.33(4) eV for oxalyl chloride. Each of these molecules is obtained by the substitutions indicated in Figure 5.6, with glyoxal being the original member of the series. The electron-donating property of methyl has a destabilizing effect on the anion, progressively reducing the electron affinity from unsubstituted glyoxal to singly substituted methylglyoxal and to doubly substituted biacetyl. In contrast, the strong electron-withdrawing

power of two very electronegative chlorine substituents in oxalyl chloride lends significant stabilization to the anion, resulting in a large ( $\sim 1$  eV) increase in the detachment energy.

## 5.6 Summary

We have investigated both experimentally and theoretically the structure of oxalyl chloride and its anion. The photoelectron spectra and angular distributions obtained at 355 and 532 nm were interpreted in terms of a transition from the ground state of the anion to the ground state of the neutral. The band's onset at  $\sim 1,8$  eV corresponds to the previously unknown adiabatic EA of oxalyl chloride and is in good agreement with the theory prediction of EA = 1.797 eV. The observed VDE of the anion, 2.33(4) eV, is also in excellent agreement with the corresponding theory predictions. The 532 nm photoelectron spectrum additionally reveals an uncharacteristically sharp onset near the photon-energy limit, assigned to autodetachment via a low-energy anionic resonance in oxalyl chloride.

These results should be viewed in the broader context of the organic substitution series, which includes glyoxal, methylglyoxal, biacetyl, and oxalyl chloride. The electron affinities and anion detachment energies in this series follow the trend: biacetyl < methylglyoxal < glyoxal  $\ll$  oxalyl chloride, which confirms the known properties of the substituents. Specifically, the electron-donating character of CH<sub>3</sub> imparts a progressively destabilizing effect on the methylglyoxal and biacetyl anions (singly- and doubly-substituted, respectively). In contrast, the strong electron-withdrawing character of Cl strongly stabilizes the anion of oxalyl chloride, resulting in a large

increase in its detachment energy, compared to that of unsubstituted glyoxal.

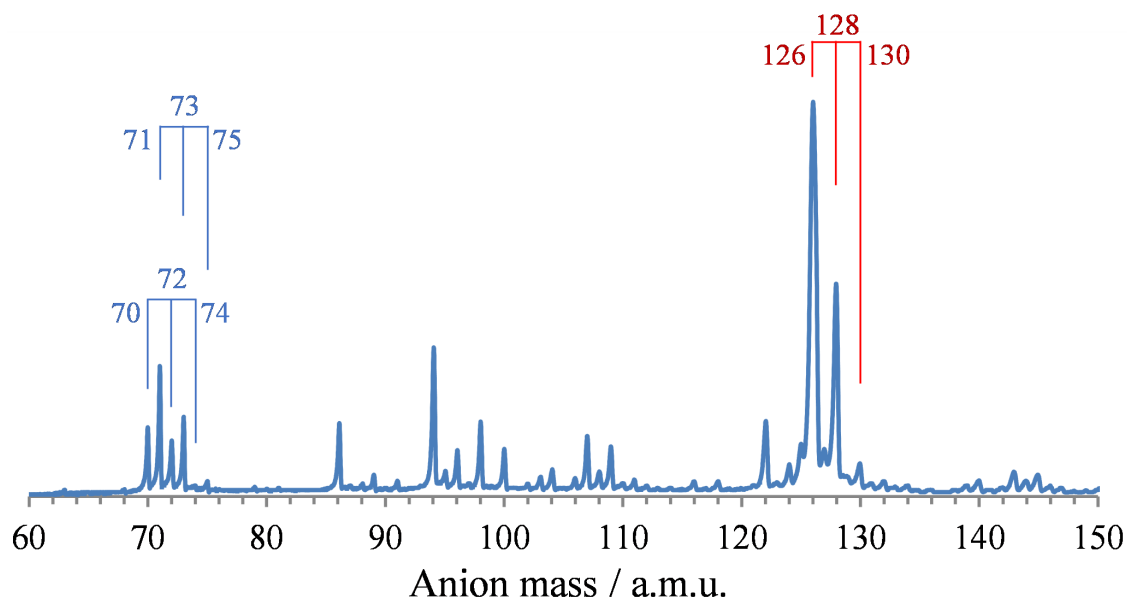


Figure 5.3: Representative parent-anion mass spectrum. Three-pronged combs indicate mass triplets corresponding to ions with two chlorine atoms. The oxalyl chloride,  $(\text{COCl})_2^-$ , triplet is  $m/z = 126 - 128 - 130$ .  $m/z = 70 - 72 - 74$  corresponds to  $\text{Cl}_2^-$  and  $m/z = 71 - 73 - 75$  to  $\text{HCl}_2^-$ . Tentative assignments of some other peaks (not marked in the figure):  $m/z = 94 - 96 - 98$  is  $(\text{CCl})_2^-$ ;  $m/z = 98 - 100 - 102$  is the anion of phosgene,  $\text{COCl}_2^-$ .

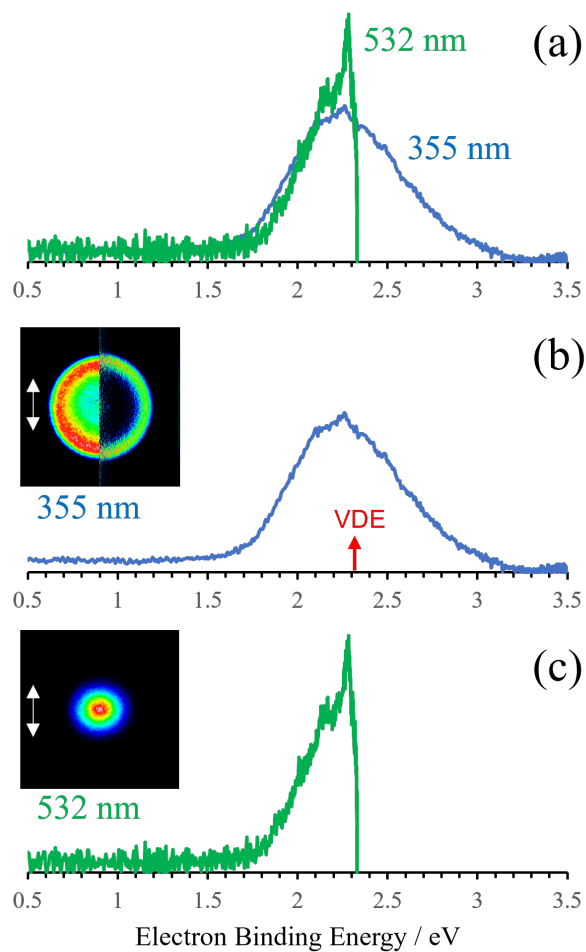


Figure 5.4: Anion photoelectron images and spectra of oxalyl chloride. (a) Overlaid 355 nm (blue) and 532 nm (green) spectra. Relative normalization is arbitrary. (b) The 355 nm photoelectron image, with the right and left halves corresponding to the raw and Abel-inverted data, respectively, and corresponding energy spectrum (blue). The vertical double arrow indicates the laser polarization direction. The red vertical arrow indicates the VDE = 2.33(4) eV. (c) The raw 532 nm photoelectron image and the corresponding energy spectrum (green).

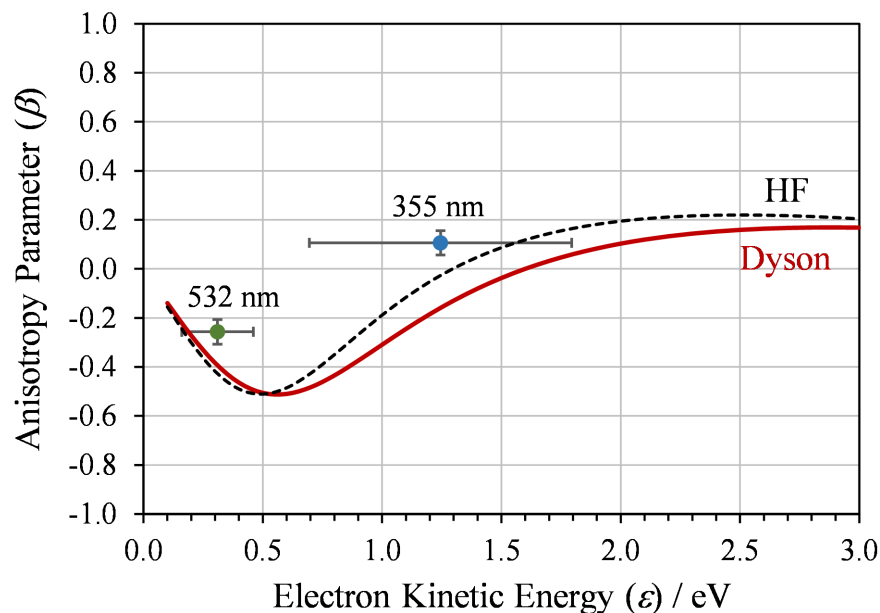


Figure 5.5: Symbols: the photoelectron anisotropy ( $\beta$ ) values determined from the 355 nm and 532 nm experimental data, plotted against the corresponding average eKEs. The large horizontal error bars indicate the respective energy ranges over which the PADs were analyzed. The vertical error bars represent the statistical uncertainties in determining the  $\beta$  values. Black dashed and red solid curves: the  $\beta(\epsilon)$  trends predicted by ezDyson based on the HF and Dyson orbitals, respectively, shown in Figure 5.1.

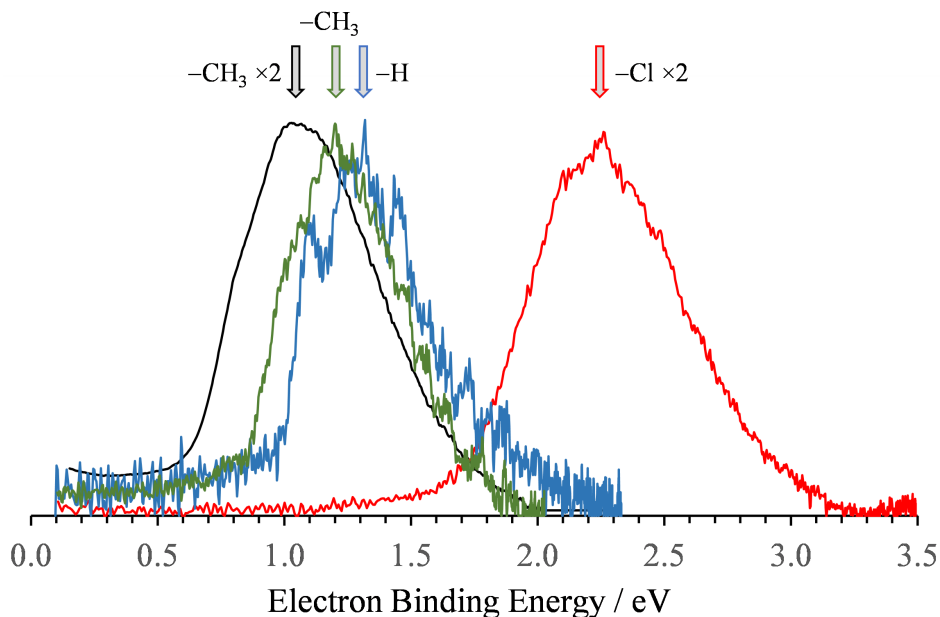


Figure 5.6: Comparison of the anion photoelectron spectra of (left to right) biacetyl (532 nm), methylglyoxal (612 nm), glyoxal (532 nm), and oxalyl chloride (355 nm). Black arrows above the spectra indicate the respective substituents:  $-\text{CH}_3$  ( $\times 2$ ) in biacetyl, a single  $-\text{CH}_3$  group in methylglyoxal,  $-\text{H}$  (i.e., no substitution) in glyoxal, and  $-\text{Cl} \times 2$  in oxalyl chloride.

# Chapter 6

## Summary and future directions

In this dissertation, we presented the study of cluster anions of BA using photoelectron imaging spectroscopy, supported by geometry optimization calculations. We showed that  $BA_2^-$  and  $BA_3^-$  have sandwich-like structures, enabled by flat geometry of BA, the excess charge being delocalized over the whole clusters. The delocalization is facilitated by the HOMO of BA through  $\pi - \pi$  interaction of  $\pi$  lobes situated along the central C-C bonds of BA molecules.

We also presented comparative study of the substitution series (Figure 1.1), which includes glyoxal, methylglyoxal (single methyl substitution), biacetyl (double methyl substitution), and oxalyl chloride (double chlorine substitution). We characterized several lowest electronic states of methylglyoxal and oxalyl chloride, and determined their EA for the first time. The EAs and anion detachment energies follow the trend: biacetyl < methylglyoxal < glyoxal  $\ll$  oxalyl chloride, confirming the destabilizing electron donating nature of methyl group and the strong electron-

withdrawing power of Cl.

As a continuation of the research presented here, one can expand the study of cluster anions of BA to larger clusters. Another option is to study cluster anions of BA in a more realistic environment, as opposed to high vacuum. For example, the clusters can be solvated by water molecules, the most common solvent in chemistry. In both cases, it will be interesting to see how much perturbation is necessary to prevent charge delocalization. A third avenue of research could be a study of cluster anions of oxalyl chloride. Oxalyl chloride has the same geometry as biacetyl and the HOMO of its anion is quite similar to the HOMO of biacetyl anion (Figures 4.7, 5.1), but its EA is almost an eV larger than EA of biacetyl. On the one hand, the high EA keeps an electron tightly bound to the oxalyl chloride anion, which seemingly precludes electron sharing between several molecules. On the other hand, it gives strong electron-withdrawing power to neutral oxalyl chloride, which may suggest formation of polymer anions.

# Bibliography

- <sup>1</sup>P. W. Anderson, “More is different”, *Science* **177**, 393–396 (1972).
- <sup>2</sup>A. J. Stone, *The theory of intermolecular forces* (Oxford University Press, Oxford, 2013).
- <sup>3</sup>F. Scheck, *Mechanics: from Newton’s laws to deterministic chaos* (Springer, Berlin, Heidelberg, 2018).
- <sup>4</sup>A. W. Castleman and K. H. Bowen, “Clusters: structure, energetics, and dynamics of intermediate states of matter”, *The Journal of Physical Chemistry* **100**, 12911–12944 (1996).
- <sup>5</sup>M. Faraday, “X. The Bakerian lecture. Experimental relations of gold (and other metals) to light”, *Philosophical Transactions of the Royal Society of London* **147**, 145–181 (1857).
- <sup>6</sup>P. Bentley, “Polymers of carbon dioxide”, *Nature* **190**, 432–433 (1961).
- <sup>7</sup>W. Z. Henkes, “Ionisierung und beschleunigung kondensierter molekularstrahlen”, *Naturforsch* **16A**, 842 (1961).
- <sup>8</sup>A. Sanov and W. Carl Lineberger, “Cluster anions: structure, interactions, and dynamics in the sub-nanoscale regime”, *Phys. Chem. Chem. Phys.* **6**, 2018–2032 (2004).

- <sup>9</sup>M. J. DeLuca, B. Niu, and M. A. Johnson, “Photoelectron spectroscopy of  $(\text{CO}_2)_n^-$  clusters with  $2 \leq n \leq 13$ : cluster size dependence of the core molecular ion”, *The Journal of Chemical Physics* **88**, 5857–5863 (1988).
- <sup>10</sup>T. Tsukuda, M. A. Johnson, and T. Nagata, “Photoelectron spectroscopy of  $(\text{CO}_2)_n^-$  revisited: core switching in the  $2 \leq n \leq 16$  range”, *Chemical Physics Letters* **268**, 429–433 (1997).
- <sup>11</sup>M. Saeki, T. Tsukuda, and T. Nagata, “Ab initio study of  $\text{CO}_2^- \cdot \text{CO}_2 \leftrightarrow \text{C}_2\text{O}_4^-$  isomerization”, *Chemical Physics Letters* **348**, 461–468 (2001).
- <sup>12</sup>M. Saeki, T. Tsukuda, and T. Nagata, “Ab initio study of  $(\text{CO}_2)_n^-$ : structures and stabilities of isomers”, *Chemical Physics Letters* **340**, 376–384 (2001).
- <sup>13</sup>R. Mabbs, E. Surber, L. Velarde, and A. Sanov, “Effects of solvation and core switching on the photoelectron angular distributions from  $(\text{CO}_2)_n^-$  and  $\text{CO}_2^- \cdot \text{H}_2\text{O}$ ”, *The Journal of Chemical Physics* **120**, 5148–5154 (2004).
- <sup>14</sup>T. Kondow and K. Mitsuke, “Formation of negative cluster ions of  $\text{CO}_2$ ,  $\text{OCS}$ , and  $\text{CS}_2$  produced by electron transfer from high-rydberg rare gas atoms”, *The Journal of Chemical Physics* **83**, 2612–2613 (1985).
- <sup>15</sup>**Y. Dauletyarov**, A. A. Wallace, C. C. Blackstone, and A. Sanov, “Photoelectron spectroscopy of biacetyl and its cluster anions”, *The Journal of Physical Chemistry A* **123**, 4158–4167 (2019).
- <sup>16</sup>T. Xue, A. R. Dixon, and A. Sanov, “Anion photoelectron imaging spectroscopy of glyoxal”, *Chemical Physics Letters* **660**, 205–208 (2016).

- <sup>17</sup>Y. Dauletyarov, A. R. Dixon, A. A. Wallace, and A. Sanov, “Electron affinity and excited states of methylglyoxal”, *The Journal of Chemical Physics* **147**, 013934 (2017).
- <sup>18</sup>Y. Dauletyarov, B. Ru, and A. Sanov, “The anion of oxalyl chloride: structure and spectroscopy”, *The Journal of Physical Chemistry A*, 1 (2021).
- <sup>19</sup>T. G. Habteyes, *Electronic structure and photochemistry of molecular and cluster anions via tandem time-of-flight mass spectroscopy and photoelectron imaging*, (Mar. 2022) <http://sanov.arizona.edu/dissertations/Habteyes2008.pdf>.
- <sup>20</sup>L. A. Velarde, *Photoinitiated dynamics of cluster anions via photoelectron imaging and photofragment mass spectroscopy*, (Apr. 2022) <http://sanov.arizona.edu/dissertations/Velarde2008.pdf>.
- <sup>21</sup>M. A. Johnson and W. C. Lineberger, “Pulsed methods for cluster ion spectroscopy”, in *Techniques for the study of ion molecule reactions*, edited by J. M. Farrar and W. H. Saunders (Wiley, New York, 1988), pp. 591–635.
- <sup>22</sup>W. C. Wiley and I. H. McLaren, “Time-of-flight mass spectrometer with improved resolution”, *Review of Scientific Instruments* **26**, 1150–1157 (1955).
- <sup>23</sup>A. T. J. B. Eppink and D. H. Parker, “Velocity map imaging of ions and electrons using electrostatic lenses: application in photoelectron and photofragment ion imaging of molecular oxygen”, *Review of Scientific Instruments* **68**, 3477–3484 (1997).
- <sup>24</sup>D. A. Dahl, “Simion for the personal computer in reflection”, *International Journal of Mass Spectrometry* **200**, 3–25 (2000).

- <sup>25</sup>A. J. R. Heck and D. W. Chandler, “Imaging techniques for the study of chemical reaction dynamics”, *Annual Review of Physical Chemistry* **46**, 335–372 (1995).
- <sup>26</sup>V. Dribinski, A. Ossadtchi, V. A. Mandelshtam, and H. Reisler, “Reconstruction of abel-transformable images: the gaussian basis-set expansion abel transform method”, *Review of Scientific Instruments* **73**, 2634–2642 (2002).
- <sup>27</sup>D. M. Neumark, K. R. Lykke, T. Andersen, and W. C. Lineberger, “Laser photodetachment measurement of the electron affinity of atomic oxygen”, *Phys. Rev. A* **32**, 1890–1892 (1985).
- <sup>28</sup>S. J. Cavanagh, S. T. Gibson, M. N. Gale, C. J. Dedman, E. H. Roberts, and B. R. Lewis, “High-resolution velocity-map-imaging photoelectron spectroscopy of the  $\text{o}^-$  photodetachment fine-structure transitions”, *Phys. Rev. A* **76**, 052708 (2007).
- <sup>29</sup>K. F. Ho, S. S. Ho, W. T. Dai, C. J. J., H. R. J., T. L., and D. W. J., “Seasonal variations of monocarbonyl and dicarbonyl in urban and sub-urban sites of xi’an, china.”, *Environ. Monit. Assess* **186**, 2835–49 (2014).
- <sup>30</sup>C. J. Kampf, A. L. Corrigan, A. M. Johnson, W. Song, P. Keronen, R. Königstedt, J. Williams, L. M. Russell, T. Petäjä, H. Fischer, and T. Hoffmann, “First measurements of reactive  $\alpha$ -dicarbonyl concentrations on  $\text{pm}_{2.5}$  aerosol over the boreal forest in finland during humppa-copec 2010 – source apportionment and links to aerosol aging”, *Atmospheric Chemistry and Physics* **12**, 6145–6155 (2012).
- <sup>31</sup>D. O. De Haan, A. L. Corrigan, M. A. Tolbert, J. L. Jimenez, S. E. Wood, and J. J. Turley, “Secondary organic aerosol formation by self-reactions of methylglyoxal and glyoxal in evaporating droplets”, *Environmental Science & Technology* **43**, 8184–8190 (2009).

- <sup>32</sup>R. Zhao, A. K. Y. Lee, and J. P. D. Abbatt, “Investigation of aqueous-phase photooxidation of glyoxal and methylglyoxal by aerosol chemical ionization mass spectrometry: observation of hydroxyhydroperoxide formation”, *The Journal of Physical Chemistry A* **116**, 6253–6263 (2012).
- <sup>33</sup>M. M. Galloway, M. H. Powelson, N. Sedehi, S. E. Wood, K. D. Millage, J. A. Kononenko, A. D. Rynaski, and D. O. De Haan, “Secondary organic aerosol formation during evaporation of droplets containing atmospheric aldehydes, amines, and ammonium sulfate”, *Environmental Science & Technology* **48**, 14417–14425 (2014).
- <sup>34</sup>J. C. Hensley, A. W. Birdsall, G. Valtierra, J. L. Cox, and F. N. Keutsch, “Revisiting the reaction of dicarbonyls in aerosol proxy solutions containing ammonia: the case of butenedial”, *Atmospheric Chemistry and Physics* **21**, 8809–8821 (2021).
- <sup>35</sup>D. C. Rawlings and E. R. Davidson, “On the electron affinity of glyoxal and methyl glyoxal”, *The Journal of Chemical Physics* **72**, 6808–6810 (1980).
- <sup>36</sup>L. H. Spangler and D. W. Pratt, “Laser-induced phosphorescence spectroscopy in supersonic jets. the lowest triplet states of glyoxal, methylglyoxal, and biacetyl”, *The Journal of Chemical Physics* **84**, 4789–4796 (1986).
- <sup>37</sup>M. Gurnick, J. Chaiken, T. Benson, and J. D. McDonald, “Vibrational and rotational spectroscopy of the first electronically allowed transition of  $\alpha$ -dicarbonyls”, *The Journal of Chemical Physics* **74**, 99–105 (1981).
- <sup>38</sup>K. M. Ervin, T. M. Ramond, G. E. Davico, R. L. Schwartz, S. M. Casey, and W. C. Lineberger, “Naphthyl radical: negative ion photoelectron spectroscopy, franck-condon simulation, and thermochemistry”, *The Journal of Physical Chemistry A* **105**, 10822–10831 (2001).

- <sup>39</sup>E. P. Wigner, “On the behavior of cross sections near thresholds”, *Phys. Rev.* **73**, 1002–1009 (1948).
- <sup>40</sup>S. Rossignol, K. Z. Aregahegn, L. Tinel, L. Fine, B. Nozière, and C. George, “Glyoxal induced atmospheric photosensitized chemistry leading to organic aerosol growth”, *Environmental Science & Technology* **48**, 3218–3227 (2014).
- <sup>41</sup>L.-M. W. Shan-Shan. PAN, “The atmospheric oxidation mechanism of *o*-xylene initiated by hydroxyl radicals”, *Acta Physico-Chimica Sinica* **31**, 2259, 2259 (2015).
- <sup>42</sup>G. Zhang, Y. Mu, L. Zhou, C. Zhang, Y. Zhang, J. Liu, S. Fang, and B. Yao, “Summertime distributions of peroxyacetyl nitrate (pan) and peroxypropionyl nitrate (ppn) in beijing: understanding the sources and major sink of pan”, *Atmospheric Environment* **103**, 289–296 (2015).
- <sup>43</sup>“Known and unexplored organic constituents in the earth’s atmosphere”, *Environmental Science & Technology* **41**, 1514–1521 (2007).
- <sup>44</sup>P. Kebarle and S. Chowdhury, “Electron affinities and electron-transfer reactions”, *Chemical Reviews* **87**, 513–534 (1987).
- <sup>45</sup>L. d. V. Moulds and H. L. Riley, “110. the polymerisation of methylglyoxal”, *J. Chem. Soc.*, 621–626 (1938).
- <sup>46</sup>E. Epifanovsky et al., “Software for the frontiers of quantum chemistry: an overview of developments in the q-chem 5 package”, *The Journal of Chemical Physics* **155**, 084801 (2021).

- <sup>47</sup>A. I. Krylov, “Equation-of-motion coupled-cluster methods for open-shell and electronically excited species: the hitchhiker’s guide to fock space”, *Annual Review of Physical Chemistry* **59**, 433–462 (2008).
- <sup>48</sup>Y. Zhao and D. G. Truhlar, “The m06 suite of density functionals for main group thermochemistry, thermochemical kinetics, noncovalent interactions, excited states, and transition elements: two new functionals and systematic testing of four m06-class functionals and 12 other functionals.”, *Theor. Chem. Account.*, 215–241 (2008).
- <sup>49</sup>L. Mohammadkhani and M. M. Heravi, “Oxalyl chloride: a versatile reagent in organic transformations”, *ChemistrySelect* **4**, 6309–6337 (2019).
- <sup>50</sup>G. Chu, J. Chen, F. Liu, X. Shan, J. Han, and L. Sheng, “Conformation-specific dissociative photoionization of oxalyl chloride in the gas phase”, *Chemical Physics* **416**, 26–32 (2013).
- <sup>51</sup>D. Holland, S. Nandi, C. Nicolas, J. Bozek, M. Patanen, and I. Powis, “An experimental and theoretical study of the valence shell photoelectron spectrum of oxalyl chloride”, *Chemical Physics* **542**, 111050 (2021).
- <sup>52</sup>J. L. Meeks and S. P. McGlynn, “Photoelectron spectra of carbonyls. oxalyl chloride, ethyl oxalyl chloride, ethyl oxamate and n,n-dimethyl ethyl oxamate”, *Spectroscopy Letters* **8**, 439–447 (1975).
- <sup>53</sup>D. Frost, C. McDowell, G. Pouzard, and N. Westwood, “The photoelectron spectra of the oxalyl halides (cox)<sub>2</sub>, [x = f, cl and br]”, *Journal of Electron Spectroscopy and Related Phenomena* **10**, 273–292 (1977).

- <sup>54</sup>B. D. Saksena and R. E. Kagarise, "Rotational isomerism in oxalyl chloride (cloc–cocl)", *The Journal of Chemical Physics* **19**, 987–993 (1951).
- <sup>55</sup>B. D. Saksena and G. S. Jauhri, "Interpretation of the ultraviolet spectrum of oxalyl chloride", *The Journal of Chemical Physics* **36**, 2233–2235 (1962).
- <sup>56</sup>A. V. Baklanov and L. N. Krasnoperov, "Oxalyl chloride a clean source of chlorine atoms for kinetic studies", *The Journal of Physical Chemistry A* **105**, 97–103 (2001).
- <sup>57</sup>M. Ahmed, D. Blunt, D. Chen, and A. G. Suits, "Uv photodissociation of oxalyl chloride yields four fragments from one photon absorption", *The Journal of Chemical Physics* **106**, 7617–7624 (1997).
- <sup>58</sup>D. D. Danielson, L. Hedberg, K. Hedberg, K. Hagen, and M. Trtteberg, "Conformational analysis. 21. the torsional problem in oxalyl chloride. an ab initio and electron diffraction investigation of the structures of the conformers and their energy and entropy differences", *The Journal of Physical Chemistry* **99**, 9374–9379 (1995).
- <sup>59</sup>K. Hagen and K. Hedberg, "Conformational analysis. i. molecular structure, composition, trans-gauche energy and entropy differences, and potential hindering internal rotation of gaseous oxalyl chloride as determined by electron diffraction", *Journal of the American Chemical Society* **95**, 1003–1009 (1973).
- <sup>60</sup>G. Chung and Y. Kwon, "Molecular structures of gauche and trans conformers for oxalyl chloride: ab initio and dft calculations", *Journal of Molecular Structure: THEOCHEM* **496**, 199–206 (2000).

- <sup>61</sup>S. Bokarev, V. Pupyshev, and I. Godunov, “Vibronic spectra, ab initio calculations, and structures of conformationally non-rigid molecules of oxalyl halides in the ground and lowest excited electronic states. part ii: theoretical investigation of oxalyl chloride”, *Journal of Molecular Spectroscopy* **256**, 247–255 (2009).
- <sup>62</sup>J. Cooper and R. N. Zare, “Photoelectron angular distributions”, in *Atomic collision processes*, edited by S. Geltman, K. T. Mahanthappa, and W. E. Brittin (Gordon and Breach, Science Publishers, New York, London, Paris, 1968), pp. 317–337.
- <sup>63</sup>K. L. Reid, “Photoelectron angular distributions”, *Annual Review of Physical Chemistry* **54**, 397–424 (2003).
- <sup>64</sup>A. Sanov, “Laboratory-frame photoelectron angular distributions in anion photodetachment: insight into electronic structure and intermolecular interactions”, *Annual Review of Physical Chemistry* **65**, 341–363 (2014).
- <sup>65</sup>P. U. Manohar and A. I. Krylov, “A noniterative perturbative triples correction for the spin-flipping and spin-conserving equation-of-motion coupled-cluster methods with single and double substitutions”, *The Journal of Chemical Physics* **129**, 194105 (2008).
- <sup>66</sup>I. Godunov, N. Yakovlev, S. Bokarev, A. Abramenzkov, and D. Maslov, “Vibronic spectra, ab initio calculations, and structures of conformationally non-rigid molecules of oxalyl halides in the ground and lowest excited electronic states. part i: reanalysis of the 3680Å and 4100Å absorption systems of oxalyl chloride”, *Journal of Molecular Spectroscopy* **255**, 39–44 (2009).
- <sup>67</sup>N. Moiseyev, *Non-hermitian quantum mechanics* (Cambridge University Press, Cambridge, 2011).

- <sup>68</sup>S. Klaiman and I. Gilary, “On resonance: a first glance into the behaviour of unstable states”, in *Advances in quantum chemistry*, Vol. 63, edited by C. A. Nicolaides, E. Brandas, and J. R. Sabin (Academic press, Cambridge, 2012), pp. 1–31.
- <sup>69</sup>H. Reisler and A. I. Krylov, “Interacting rydberg and valence states in radicals and molecules: experimental and theoretical studies”, *International Reviews in Physical Chemistry* **28**, 267–308 (2009).
- <sup>70</sup>K. Sneskov and O. Christiansen, “Excited state coupled cluster methods”, *WIREs Computational Molecular Science* **2**, 566–584 (2012).
- <sup>71</sup>D. Zuev, T.-C. Jagau, K. B. Bravaya, E. Epifanovsky, Y. Shao, E. Sundstrom, M. Head-Gordon, and A. I. Krylov, “Complex absorbing potentials within eom-cc family of methods: theory, implementation, and benchmarks”, *The Journal of Chemical Physics* **141**, 024102 (2014).
- <sup>72</sup>T.-C. Jagau, D. Zuev, K. B. Bravaya, E. Epifanovsky, and A. I. Krylov, “A fresh look at resonances and complex absorbing potentials: density matrix-based approach”, *The Journal of Physical Chemistry Letters* **5**, 310–315 (2014).
- <sup>73</sup>T. Seideman, “Time-resolved photoelectron angular distributions: a nonperturbative theory”, *The Journal of Chemical Physics* **107**, 7859–7868 (1997).
- <sup>74</sup>C. M. Oana and A. I. Krylov, “Cross sections and photoelectron angular distributions in photodetachment from negative ions using equation-of-motion coupled-cluster dyson orbitals”, *The Journal of Chemical Physics* **131**, 124114 (2009).
- <sup>75</sup>R. Mabbs, E. R. Grumbling, K. Pichugin, and A. Sanov, “Photoelectron imaging: an experimental window into electronic structure”, *Chem. Soc. Rev.* **38**, 2169–2177 (2009).

<sup>76</sup>A. I. Krylov, “From orbitals to observables and back”, *The Journal of Chemical Physics* **153**, 080901 (2020).

<sup>77</sup>S. Gozem and A. I. Krylov, “The ezspectra suite: an easy-to-use toolkit for spectroscopy modeling”, *WIREs Computational Molecular Science* **12**, e1546 (2022).

<sup>78</sup>S. Gozem, A. O. Gunina, T. Ichino, D. L. Osborn, J. F. Stanton, and A. I. Krylov, “Photoelectron wave function in photoionization: plane wave or coulomb wave?”, *The Journal of Physical Chemistry Letters* **6**, 4532–4540 (2015).